Acta Materialia 266 (2024) 119645

Contents lists available at ScienceDirect

Acta Materialia

journal homepage: www.elsevier.com/locate/actamat

Full length article

Combining crystal plasticity and phase field model for predicting texture evolution and the influence of nuclei clustering on recrystallization path kinetics in Ti-alloys

Arunabha M. Roy [a,*], Sriram Ganesan [b], Pinar Acar [c], Raymundo Arróyave [a,d], V. Sundararaghavan [b]

[a] Department of Materials Science and Engineering, Texas A&M University, 3003 TAMU, College Station, TX 77843, USA
[b] Aerospace Engineering, University of Michigan, Ann Arbor, MI 48109, USA
[c] Department of Mechanical Engineering, Virginia Tech, Blacksburg, VA, 24061, USA
[d] Department of Mechanical Engineering, Texas A&M University, 3003 TAMU, College Station, TX 77843, USA

ARTICLE INFO

Keywords:
Static recrystallization
Crystal plasticity
Orientation distribution function
Phase field
Texture and microstructure evolution
Avrami kinetics

ABSTRACT

A three-dimensional computational framework has been developed combining a crystal plasticity (CP) and a phase-field (PF) approach that can efficiently simulate static recrystallization (SRX) and grain growth during the hot-forming in Ti-alloys. In the framework, the CP slip system parameters have been accurately calibrated by solving an inverse optimization problem from available experimental tension and compression stress–strain data through CP simulations performed via an orientation distribution function (ODF)-based computational model. Using the CP model, the evolution of inhomogeneous local deformation, deformed texture, and grain dislocation density have been simulated in the plastically deformed polycrystalline Ti-alloys. The PF model then predicts microstructure evolution and kinetics of SRX from CP-informed dislocation density during the annealing phase. Experimental information on microstructural heterogeneity in terms of the initial arrangement of nuclei distribution has been used to guide the development of the framework that can provide deeper insights into unique morphological evolution for various types of grain impingement as well as experimental validation of SRX kinetics. Finally, when the proposed model has been quantitatively validated through experimentally measured texture evolution and SRX path kinetics, excellent agreement is achieved. The current study highlights a systematic modeling framework that is capable of predicting crystallographic texture, microstructural evolution, and kinetics in the course of SRX for a clear understanding of the relationship between the mechanical properties, various microstructural descriptors, and thermo-mechanical process in the regime of material design.

1. Introduction

Polycrystalline titanium (Ti)-alloys have been traditionally used as an extremely strong yet lightweight material with exceedingly well corrosion-resistant capability in various naval and aerospace applications [1,2]. In general, one of the common processing routes chosen for Ti-alloys is hot forging, during which the material undergoes a variety of hot rolling processes, followed by heat treatment via annealing [3,4]. Deformation prior to annealing leads to escalating the formations of dislocations and increases the stored energy of the grains which drives the nucleation process and growth of new, strain-free grains upon subsequent annealing [5,6]. During such process, the polycrystalline materials drastically change their microstructural morphology through several phenomena such as static recrystallization (SRX), grain growth, recovery, and multiple phase transitions (PTs) [3,4] that significantly alter microstructure characteristics, dislocation structures, and grain orientation [7–9]. Since the process of SRX and grain growth has a large impact on the mechanical properties of the Ti-alloys, therefore, it is critical to understand and control the influence of thermo-mechanical processes on SRX microstructures, and corresponding material properties that can facilitate developing high-performance materials for various engineering applications [10,11].

In general, SRX has been known to originate from deformation-induced microstructural inhomogeneities (i.e, grain boundaries, transition bands, shear bands) where non-homogeneously distributed dislocations in the subgrains are the main driving force for SRX nucleation [7,12]. Therefore, realistic physics/mechanics-based modeling of

* Corresponding author.
E-mail addresses: royam@tamu.edu, arunabhr.umich@gmail.com (A.M. Roy).

https://doi.org/10.1016/j.actamat.2023.119645
Received 28 July 2023; Received in revised form 20 December 2023; Accepted 29 December 2023
Available online 2 January 2024

the deformation mechanisms and SRX microstructural evolution are critical for accurate prediction of post-annealing mechanical properties of the materials [3,7,13]. During SRX, due to excessively high mechanical deformation prior to heat treatment, the grains are plastically deformed. To this end, the approach of mesoscale mechanical models such as crystal plasticity (CP) is a powerful method to link the mechanical properties of heterogeneous materials with the evolution of SRX grains that can provide dislocation evolution under plastic deformation [14]. Equipped with physics-based constitutive theories [14–18], it incorporates physics-based deformation mechanisms employing dislocation density-based hardening models [19–21] into CP framework for realistic dislocation activities and structures. Due to the ability to predict spatial dislocation and texture evolution of the deformed polycrystalline microstructure, CP is a powerful numerical procedure for analyzing the deformation of crystalline materials at different length scales [22–27]. In the last decades, several studies on Ti-alloys have been performed utilizing various CP models [28–33] that demonstrates its excellent capability of predicting in-homogeneity of the deformed microstructure as well as texture evolution [15,22,34,35]. Along a similar line, CP modeling with orientation distribution function (ODF) is an efficient alternative to computationally expensive finite element (FE) methods. The ODF can be defined based on a parameterization of the crystal lattice rotation such as Euler-angle representations [36,37], and Rodrigues parameterization [38]. Conversion of continuous orientation space to finite degrees of freedom requires discretization techniques which can be based on either a global basis utilizing spherical harmonics or Fourier space [39,40], or a local basis employing FE discretized Rodrigues space with locally defined polynomial shape functions [41,42]. Recently, utilizing optimum design parameters, ODF-based micromechanical modeling has been used to predict grain orientations and uncertainty quantification of microstructural properties in Ti-alloys [43,43–50].

Although CP models can successfully simulate grain level deformations and texture evolution for polycrystalline materials, however, capturing SRX complex microstructure evolutions is quite challenging which is predominately driven by the migration of grain boundaries during various thermo-mechanical processing [3]. In recent years, various mesoscale computational techniques, notably, Monte-Carlo (M-C) [51,52], cellular automata (CA) [53,54] have been developed accounting for the evolution of grain structures to model SRX and grain growth. Subsequently, the phase-field (PF) method has been widely applied to model various mesoscale phenomena [55–57], in particular, solid-solid PTs via intermediate melting [58–62], solidification [63], recrystallization [64–69], and grain growth [70,71]. In order to simulate the evolution of complex microstructural morphological evolution on the real temporospatial scale, PF models are much more advantageous compared to other models since the influence of interface/grain-boundary curvature does not need to track explicitly during the evolution [72,73]. Thus, PF models are particularly suitable for SRX microstructure evolution where morphological complexities are common [70,71]. To this end, the PF model for grain growth has been developed accounting for the arbitrary misorientation and inclination dependence of the grain boundary properties for anisotropic systems [74–77]. More recently, a PF model for SRX has been developed where the volume fraction of SRX has been quantified via Avirami kinetics for pure-Ti [68,69]. It is noteworthy to mention that most of the existing PF models for SRX incorporate the strain energy contribution to microstructure evolution in the elastic regime. However, proper thermo-mechanical modeling of SRX requires driving forces resulting from the plastic activities which is critical for accurately predicting the microstructure evolution and kinetics of SRX.

With the recent advancement of material modeling at multiple length scales, significant efforts have been persuaded to couple CP with different microstructure evolution models [78,79]. In [80], CP has been combined with a probabilistic kinetics-based CA approach to model recrystallization. Subsequently, the M-C method has been integrated with CP to predict particle simulated nucleation (PSN) during recrystallization in Al-alloys [81,82]. More recently, PF models have been combined with the CP framework to capture grain boundary sliding, migration of grain structure, the effect of strain rate on dynamic recrystallization (DRX), and grain growth [83–85]. In terms of SRX, several attempts have been made to integrate the PF method with CP at the mesoscale. In this context, the dislocation density-based CP model has been used assuming a homogeneous dislocation density field in each grain to simulate SRX [64,65]. Furthermore, cold-rolling and annealing of steel during SRX have been simulated by coupling the CP and PF models [86]. In a separate work, a CP and PF model has been combined to study SRX microstructural evolution in pure Al [12]. More recently, CP and PF models have been integrated for predicting SRX texture and anisotropic mechanical properties of cold-rolled carbon steels [7].

1.1. Motivations

However, the aforementioned models are mostly limited to two-dimension and relatively smaller numbers of grains which may not be suitable for accurately predicting SRX, in particular, experimentally observed texture, microstructure, and kinetics of grain growth during thermo-mechanical processing. In addition, to capture the correct deformation behavior in heterogeneous α- titanium alloy, the accurate calibration of various slip system parameters from the experimental stress–strain response is critical. To this end, a proper optimization procedure is needed for calibrating the basal, prismatic, pyramidal slip system, and twin parameters for CP using the available experimental tension and compression stress–strain data that poses a unique challenge. Such an optimization procedure has yet to be systematically addressed in the current state-of-the-art modeling approaches for complex heterogeneous α- titanium alloys, in particular Ti-07Al, as per the authors's best knowledge. Additionally, incorporating experimentally consistent initial grain structure and EBSD grain orientation data into the CP model is equally important to predict the evolution of post-annealing deformation texture and dislocation density (or stored energy) distributions in the deformed polycrystalline Ti-alloys. Besides, the experimental EBSD images of partially SRX microstructures in Ti-alloys such as Ti-0Al (pure Ti) and Ti-7Al indicate the presence of initial bands of clustered nuclei (or SRX grains) [87]. Contrary to the random nucleation assumption mostly used in literature [7,64,65], the non-homogeneous distribution of SRX grains does not conform to Avirami-type growth kinetics. Therefore, it cannot correctly predict experimentally observed SRX kinetics for these cases which has not been systemically explored yet. Such clustering of SRX grains influences the kinetics of the SRX process significantly by altering recrystallized microstructural morphology and the grain size distribution [88,89]. However, the existing state-of-the-art frameworks, in general, do not account for the variability in spatial distribution of nucleation sites which plays a critical role in dictating growth kinetics and corresponding microstructural path dynamics during SRX. Therefore, it is important to construct a systematic modeling framework accounting for material heterogeneity, in particular, characterizing experimentally observed various arrangements of nuclei distribution on the microstructure and validating experimentally observed recrystallization path kinetics of SRX for a better understanding of the relationship between microstructure, kinetics, and thermomechanical process in the Ti-alloys.

1.2. Contributions

To overcome the aforementioned issues, in the present work, we develop a comprehensive integrated computational materials engineering workflow. We call it as CP-PF-SRX framework combining CP and PF models that can efficiently simulate three-dimensional SRX and grain

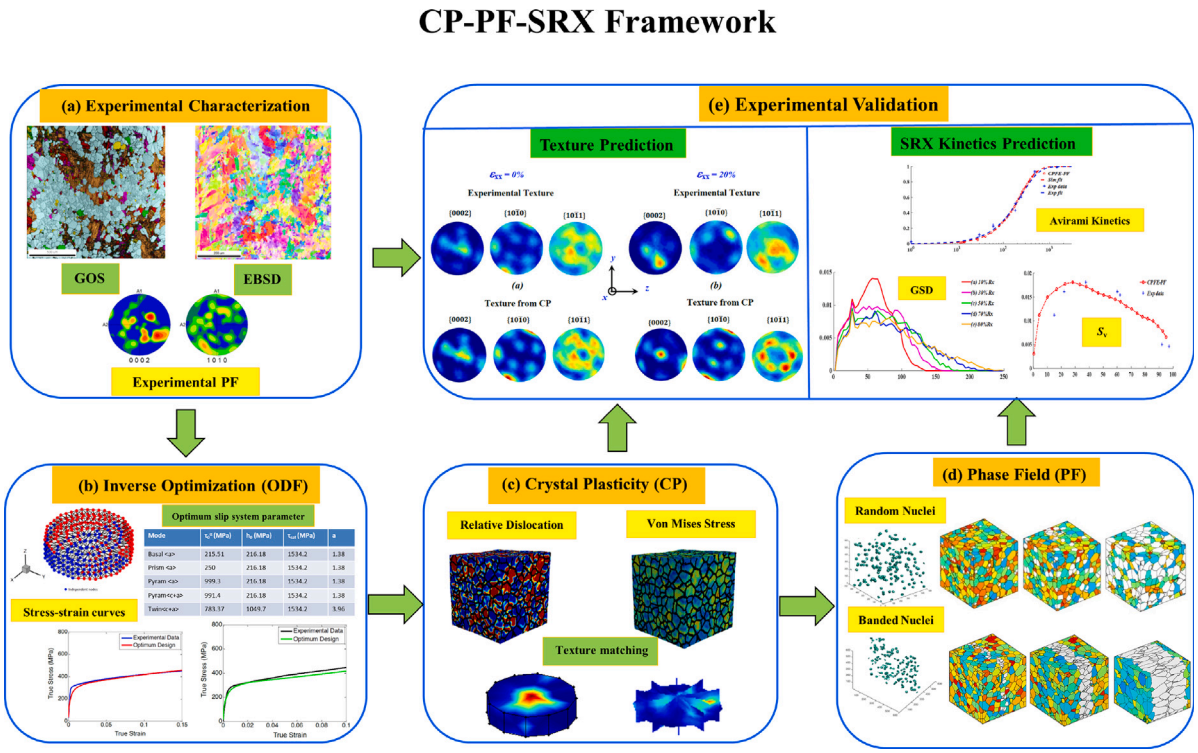

Fig. 1. Overall flowchart of proposed CP-PF-SRX : (a) experimental characterization ; (b) ODF-based inverse optimization methods; (c) CP simulation for dislocation evolution; (d) PF simulation for various nuclei arrangements; (e) textural prediction and SRX kinetics with experimental validation.

growth during the hot forming of Ti-alloys. In CP-PF-SRX, we integrate both computational and experimental efforts that can predict texture evolution in plastically deformed polycrystalline Ti-alloys during the deformation phase as well as SRX microstructure evolution, growth kinetics, and various other important microstructural descriptors during annealing phase based on experimentally observed microstructural heterogeneity and processing history. In the framework, the slip system parameters for both Ti-0Al and Ti-7Al alloys have been calibrated from available experimental tension and compression stress–strain data by solving an inverse optimization problem through CP simulations via an ODF-based computational model. A representative volume element (RVE) with equiaxed grain size and shape matching with the experimentally measured grain origination (defined by the ODF) has been used as the initial condition for the both CP and PF models. Using a three-dimensional CP model, the evolution of deformation texture as well as the spatial distribution of grain dislocation density has been predicted in the deformed polycrystalline Ti-alloys. The CP-informed dislocation density of plastically deformed microstructure before the annealing phase was then used as input for the stored energy in the grains of the initial PF model to simulate SRX and grain growth. Experimental information on microstructural heterogeneity in terms of the initial arrangement of nuclei distribution has been used to guide the development of the PF model that provide insights into unique morphological evolution for various type of grain impingement as well as experimental validation of SRX kinetics. PF microstructural evolution for both randomly nucleated and bands of clustered SRX nuclei has been compared to shed light on the uniform and non-uniform impingement kinetics and various microstructural path descriptors. The novelty of the present CP-PF-SRX modeling approach is represented by comparing the evolution of post-annealing deformation texture with the experimental results. Finally, when the experimental study on SRX for Ti-7Al is compared with the simulation results from the CP-PF-SRX model, excellent agreement is achieved. The overview of the CP-PF-SRX has been shown in Fig. 1 that includes - (a) experimental characterization ; (b) finding optimal CP slip system parameters through inverse optimization methods; (c) CP simulation for dislocation evolution; (d) PF simulation utilizing CP informed grain dislocation data; and finally (e) experimental validation with texture prediction and SRX kinetics from CP and PF models, respectively. The developed framework herein is capable of predicting crystallographic texture, complex microstructural evolution, and kinetics of SRX that would significantly advance our understanding of the relationship between the various thermo-mechanical processes during SRX. The rest of the paper is organized as follows: Section 2 details the material and experimental procedure for Ti-alloys; Section 3 describes ODF based CP model for calibration of various slip system parameters for Ti-alloys. Section 4 introduces the rate-independent CP finite element model; PF model for SRX and grain growth has been detailed in Section 5; Sections 6 and 7 deal with the relevant findings and discussion of the proposed framework, respectively. Finally, the conclusions of the current work have been outlined in Section 8.

2. Material and experimental procedure

The as received material for the current study are two different binary α titanium alloys: Ti-0Al and Ti-7Al that have been forged above the β transus temperature and then air cooled. From the as-received ingot, the cylindrical samples of size 6 mm diameter × 9 mm height were machined using electro-discharge machining (EDM) and compressed to a 20% height reduction at a steady strain rate of 0.03 mm/min (5×10^{-5} s^{-1}) at room temperature [87]. The samples were then heated in a ceramic tube furnace at 800 °C for varying times up to 24 h and subsequently water quenched to observe the effect of alloy composition on static recrystallization. Utilizing a Tescan Mira 3 scanning electron microscope (SEM), electron backscatter diffraction (EBSD) was performed using an average step size of 3 μm and an average scan area of 1500 μm × 1500 μm to obtain the fraction of recrystallization, grain size, and texture. The EBSD scans from the recrystallization studies were partitioned so that only grains with a grain orientation spread (GOS) value of less than or equal to 1° remained in order to

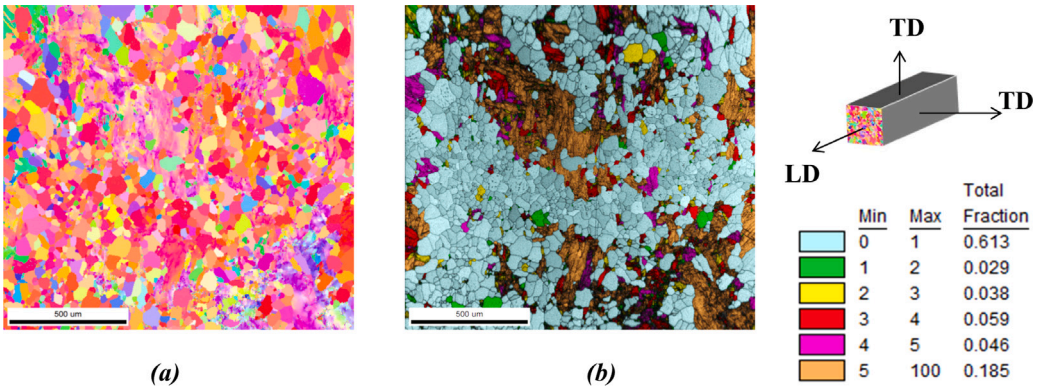

Fig. 2. (a) Experimental EBSD inverse pole figure image (IPF); (b) Grain orientation spread (GOS) map of showing the emergence of the recrystallized grain of volume fraction $R_x = 61.3\%$ in Ti-7Al sample compressed to 20% strain at room temperature and annealed at 800 °C for 18 h [87].

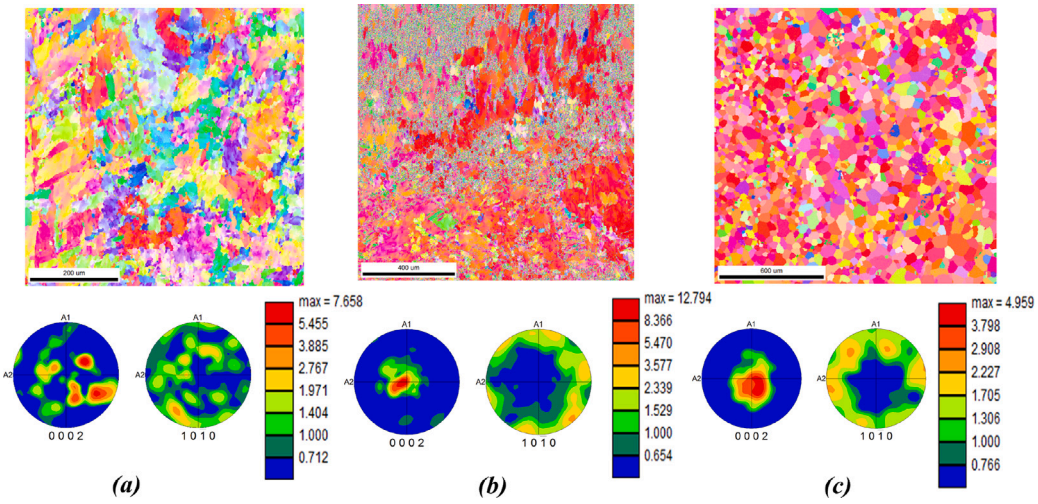

Fig. 3. Experimental EBSD inverse pole figure images (top) and corresponding pole figures (PFs) (bottom) of Ti alloys for (a) as received β cogged sample; (b) after compression of 20% strain at room temperature; (c) after recrystallization annealed at 800 °C [87].

visualize only the recrystallized grains. Using Image J software, the unimpinged grain boundaries of the recrystallized grains or the grain boundaries between the recrystallized and non-recrystallized regions were selected and the perimeter was measured. This perimeter value was then divided by the area of the whole scan region to obtain the free surface area fraction (S_v) value. The fraction recrystallized of each sample was determined by creating GOS maps from each EBSD scan which measures the local misorientation spread within each grain. A GOS value has been assigned to each grain and calculated as the average misorientation between each data point in the grain and the average orientation of all the data points within the grain. Grains with high GOS values are considered to be not recrystallized while grains with GOS values of less than 1° are considered to be recrystallized and the area fraction of recrystallized grains is used as the fraction recrystallized for that particular sample. For the Ti-7Al sample shown in Fig. 2, the recrystallized grains have been highlighted in light blue corresponding to the bin of GOS values of 0 to 1°. In Fig. 3, the texture evolution during recrystallization in β-cogged Ti-alloys which was compressed to 20% strain and then annealed at 1073 K (800 °C) has been shown [87].

In order to study grain growth, the cylindrical samples were first compressed in the same manner as for recrystallization studies. The samples then underwent a recrystallization heat treatment for 8 h at 800 °C and were water quenched in order to produce a fully recrystallized microstructure. This allows for the study of grain growth kinetics only by not including any effects from the recrystallization kinetics. The samples were then subsequently heat treated at 800 °C for various times up to 24 h and water quenched. The same sectioning, mounting, and polishing procedure was performed followed by etching using Kroll's reagent (nitric acid, hydrofluoric acid, and water) for approximately 40 s. Samples were then imaged optically using cross-polarization and the line intercept method was used to measure the average grain size.

3. Crystal plasticity finite element model

In the present work, the rate-independent crystal plasticity (CP) finite element model has been employed utilizing PRISMS-Plasticity framework [90,91]. In the CP model, a single-crystal plasticity theory [90,92] has been used for modeling the plastic deformation response of each grain. In this theory, it has been assumed that plastic flow occurs through slip mechanism on prescribed slip systems. Let us consider a material where slip systems can be defined by orthonormal vector pairs $(\boldsymbol{m}_0^\alpha, \boldsymbol{n}_0^\alpha)$ where $\boldsymbol{m}_0^\alpha$, $\boldsymbol{n}_0^\alpha$ represents slip direction and slip plane normal, respectively with slip systems $\alpha = 1, \ldots, N$ at time $t = 0$. Expressing all quantities in a crystal lattice coordinate system, the following basic fields are related by the constitutive equations: the deformation gradient $\boldsymbol{F}$, Cauchy stress $\boldsymbol{\sigma}$ and slip resistances $s^\alpha > 0$. The quantity $\boldsymbol{F}$ can be defined in the undeformed initial crystal orientation decomposing into $\boldsymbol{F} = \boldsymbol{F}^e \boldsymbol{F}^p$ (with $\det(\boldsymbol{F}^p) = 1$) where $\boldsymbol{F}^e$ and $\boldsymbol{F}^p$ are the elastic and plastic parts, respectively. In the constitutive relation, the Green elastic strain measure $\bar{\boldsymbol{E}}^e = \frac{1}{2}\left(\boldsymbol{F}^{eT}\boldsymbol{F}^e - \boldsymbol{I}\right)$ has been defined on the plastically deformed and unstressed (relaxed) configuration denoted

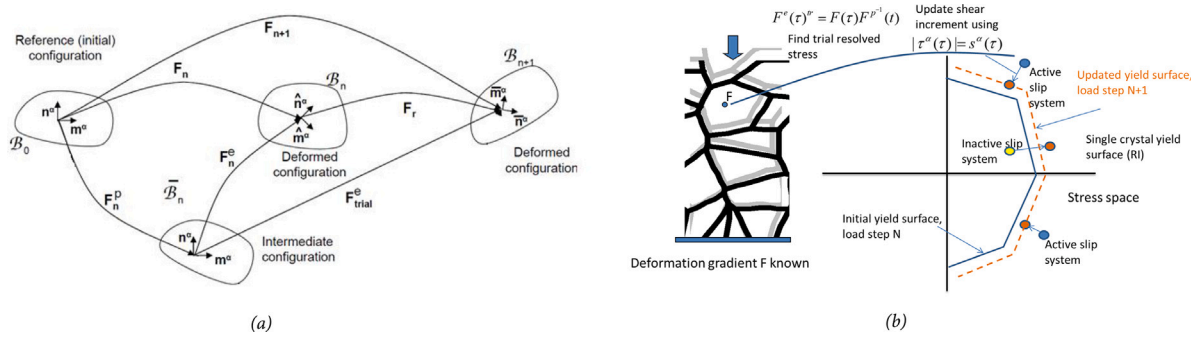

(a) (b)

Fig. 4. (a) Schematic representation of various material configurations for a single crystal constitutive model where $(\boldsymbol{m}^\alpha, \boldsymbol{n}^\alpha)$, $(\hat{\boldsymbol{m}}^\alpha, \hat{\boldsymbol{m}}^\alpha)$, and $(\bar{\boldsymbol{m}}^\alpha, \bar{\boldsymbol{n}}^\alpha)$ are the slip systems on the initial configuration $\mathcal{B}_n$ and deformed configurations $\mathcal{B}_n$, and $\mathcal{B}_{n+1}$, respectively. (b) Schematic representation of the yield surface computation and the active slip systems.

by $\bar{\mathcal{B}}$. Subsequently, the conjugate stress measure $\bar{\boldsymbol{T}}$ can be defined as $\bar{\boldsymbol{T}} = \det\boldsymbol{F}^e(\boldsymbol{F}^e)^{-1}\boldsymbol{\sigma}(\boldsymbol{F}^e)^{-T}$. The schematic diagram of the different configurations has been depicted in Fig. 4.

For stress, the constitutive relation can be expressed as $\bar{\boldsymbol{T}} = \boldsymbol{\mathcal{L}}^e\left[\bar{\boldsymbol{E}}^e\right]$ where $\boldsymbol{\mathcal{L}}^e$ is the fourth-order anisotropic elasticity tensor. Assuming dislocation glide is the mechanism for primary deformation, the evolution of the plastic velocity gradient can be expressed as

$$\boldsymbol{L}^p = \dot{\boldsymbol{F}}^p(\boldsymbol{F}^p)^{-1} = \sum_\alpha \dot{\gamma}^\alpha \boldsymbol{S}_0^\alpha sign(\tau^\alpha) \tag{1}$$

where $\dot{\gamma}^\alpha$ represents the plastic shearing rate on the α^{th} slip system; $\boldsymbol{S}_0^\alpha = \boldsymbol{m}_0^\alpha \otimes \boldsymbol{n}_0^\alpha$ is known as Schmid tensor. From such a definition, the resolved stress on the α^{th} slip system can be obtained as $\tau^\alpha = \bar{\boldsymbol{T}} \cdot \boldsymbol{S}_0^\alpha$.

The single crystal model has been solved by employing a rate-independent algorithm. For the activation of slip for a particular slip plane, the resolved shear stress τ^α must overcome a critical value that is the slip system resistance s^α. During slip, the active systems experience a plastic shearing rate $\dot{\gamma}^\alpha > 0$. Whereas, $\dot{\gamma}^\alpha = 0$ for the inactive slip systems where the resolved shear stress could not overcome s^α. The governing equation of slip resistances can be expressed as follows:

$$\dot{s}^\alpha(t) = \sum_\beta h^{\alpha\beta}\dot{\gamma}^\beta(t), \text{ with } s^\alpha(0) = \tau_0^\alpha \tag{2}$$

$$h^{\alpha\beta}(t) = \begin{cases} h_o^\beta\left(1 - \frac{s^\beta(t)}{s_s^\beta}\right)^a, & \text{if } \alpha = \beta, \quad \text{or for coplanar systems} \\ h_o^\beta q\left(1 - \frac{s^\beta(t)}{s_s^\beta}\right)^a, & \text{otherwise.} \end{cases}$$

where, $h^{\alpha\beta}$ is the slip system hardening term, τ_0^α represents the initial slip system resistance on the α^{th} slip system and $\dot{\gamma}^\beta$ is the plastic shearing rate on the β^{th} slip system. The rate-independent model is used to find the Piola–Kirchhoff-I stress, $\boldsymbol{P} = (\det\boldsymbol{F})\boldsymbol{\sigma}\boldsymbol{F}^{-T}$ and tangent modulus for getting the finite element nodes displacement. The tangent modulus $\frac{\partial \boldsymbol{P}}{\partial \boldsymbol{F}}$ for use in the weak form is computed using a fully implicit algorithm [90]. Once the CP simulation is performed, the flow stress σ_s can be obtained from the relationship between the yield stress σ_Y of strained material and the corresponding average dislocation density ρ_{ave} as follows:

$$\sigma_s = \sigma_Y + \alpha G b\sqrt{\rho_{ave}} \tag{3}$$

where G is the shear modulus; burgers vector b represents the magnitude of an $\vec{a}$ dislocation. Finally, the effective or relative dislocation density ρ_e^{CP} of the grains are obtained using the proportionality relation between the dislocation density and flow stress i.e., $\rho \propto (\sigma_s - \sigma_Y)^2$ as follows:

$$\rho_e^{\text{CP}} := \frac{\rho}{\rho_{ave}} = \frac{(\sigma_s - \sigma_Y)^2}{(\sigma_s - \sigma_Y)^2_{avg}} \tag{4}$$

In the present study, the texture of the deformed sample and CP prediction have been compared for both Ti-0Al and Ti-7Al (see Section 6.4). To provide a realistic distribution of stored energy in the PF model, before annealing, the evolution of dislocation density of plastically deformed microstructure has been extensively analyzed from the CP model (see Section 6.5).

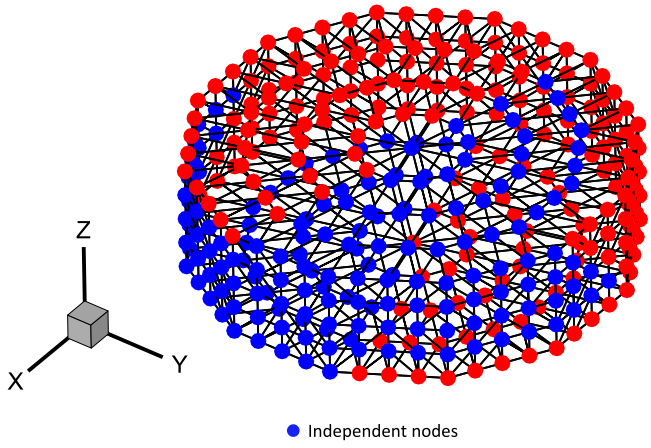

Fig. 5. Representation of ODF showing the location of the independent nodes (k = 388) in the Rodrigues fundamental region of the ODF (blue color). Each nodal point represented in the figure shows a particular crystallographic orientation, where each independent nodal point (blue nodes) is assigned to a unique ODF value to describe the corresponding crystallographic orientation. The dependent nodes (red color) demonstrate equivalent ODF values due to crystallographic symmetries in the HCP mesh representation. (For interpretation of the references to colour in this figure legend, the reader is referred to the web version of this article.)

4. Crystal plasticity modeling with orientation distribution function

The slip system parameters used in the CP model for the Ti-Al alloys i.e., Ti-0Al and Ti-7Al have been identified through an inverse optimization problem using the experimental global stress–strain curves. The CP simulations for parameter prediction have been performed with an Orientation Distribution Function (ODF) based computational model. The ODF $A(r)$ can be represented by a one-point probability measure which quantifies the volume fractions of the crystals in the orientation space, r. In the present study, FE modeling has been implemented to discretize the ODFs over the Rodrigues space. Considering crystal symmetries, the polycrystal orientation space can be reduced to a smaller subset called the fundamental region as shown in Fig. 5. Each crystal orientation within the fundamental region $\mathcal{R}$ can be represented by a unique coordinate, $\boldsymbol{r}$ which quantifies the rotation including Rodrigues vector, Euler angles, etc. The ODF $\mathcal{A}(\boldsymbol{r})$ represents the volume density of crystals of orientation $\boldsymbol{r}$. As shown in Fig. 5, $\mathcal{R}$ can be discretized into N nodes consisting of N_e elements with N_{in} integration

points in each element. The normalized ODF over the fundamental region can be expressed as:

$$\int_{\mathcal{R}} \mathcal{A} dv = \sum_{n=1}^{N_e} \sum_{m=1}^{N_{in}} A(\boldsymbol{r}_m) w_m |J_n| \frac{1}{(1+\boldsymbol{r}_m \cdot \boldsymbol{r}_m)^2} = 1 \tag{5}$$

where $A(\boldsymbol{r}_m)$ represents ODF at integration point m of the nth element with global coordinate $\boldsymbol{r}_m$; w_m is the weight associated with integration point m; $|J_n|$ is the Jacobian determinant of the element n. This is equivalent to the linear constraint: $\boldsymbol{q}^{in^T} \boldsymbol{A}^{in} = 1$, where $q_k^{in} = w_k |J_k| \frac{1}{(1+r_k \cdot r_k)^2}$ and $A_k^{in} = A(\boldsymbol{r}_k)$, where $k = 1, \ldots, N_{in} \times N_e$. With given single crystals orientation-dependent property $\chi(\boldsymbol{r})$, the average polycrystal property over the ODF can be expressed as:

$$\langle \chi \rangle = \int \chi(\boldsymbol{r}) \boldsymbol{A}(\boldsymbol{r}) dv \tag{6}$$

In linearized form, Eq. (6) can be expressed as

$$\langle \chi \rangle = \int_{\mathcal{R}} \chi(\boldsymbol{r}) \, \mathcal{A}(\boldsymbol{r}) dv \quad = \sum_{n=1}^{N_e} \sum_{m=1}^{N_{in}} \chi(\boldsymbol{r}_m) A(\boldsymbol{r}_m) w_m |J_n| \frac{1}{(1+\boldsymbol{r}_m \cdot \boldsymbol{r}_m)^2} \tag{7}$$

Which is equivalent to linearizing ODF : $\langle \chi \rangle = \boldsymbol{p}^{in^T} \boldsymbol{A}^{in}$, where $p_k^{in} = \chi(\boldsymbol{r}_k) w_k |J_k| \frac{1}{(1+r_k \cdot r_k)^2}$ and $A_k^{in} = A(\boldsymbol{r}_k)$, $k = 1, \ldots, N_{in} \times N_e$. Utilizing reduced integration considering one integration point at local coordinate $(0.25, 0.25, 0.25)$ per element and an integration weight $w = \frac{1}{6}$, the simplified $\boldsymbol{q}^{in}$ can be expressed as :

$$\boldsymbol{q} = \begin{bmatrix} \frac{1}{6}|J_1| \frac{1}{(1+r_1 \cdot r_1)^2} \\ \frac{1}{6}|J_2| \frac{1}{(1+r_2 \cdot r_2)^2} \\ \cdots \\ \frac{1}{6}|J_{N_e}| \frac{1}{(1+r_{N_e} \cdot r_{N_e})^2} \end{bmatrix}$$

In the formulation, the crystallographic symmetry can be ensured considering independent nodal points instead of the integration points. Moreover, accounting for symmetry conditions as shown in Fig. 5, the number of independent nodal points can be reduced. The ODFs at the nodal points of the FE mesh can be computed by considering $\boldsymbol{H}$ such that $\boldsymbol{A}^{in} = \boldsymbol{H} \boldsymbol{A}^n$ where $\boldsymbol{A}^n$ represents the independent nodal values. The matrix $\boldsymbol{H}$ can be obtained from $A_e^{in} = 0.25 \sum_{k=1}^{4} A_e^k$ where A_e^{in} and A_e^k, $k = 1, \ldots, 4$ represent integration point ODFs and nodal point ODFs of the tetrahedral element e, respectively. The normalization condition for the ODFs can be written as $\boldsymbol{q}^T \boldsymbol{A} = 1$ using the nodal-point ODF values. The crystal orientations from the EBSD have been binned pixel-by-pixel at the integration points. After binning, the ODF A_k^{in} contains the total number of pixels in the EBSD image that have orientations lying within the element normalized by $\boldsymbol{q}^{int^T} \boldsymbol{A}^{int}$. The matrix $\boldsymbol{T}$ has been used to convert $\boldsymbol{A}^{in}$ to $\boldsymbol{A}^n$, i.e., $\boldsymbol{A}^{node} = \boldsymbol{T} \boldsymbol{A}^{int}$. The matrix $T_{lk} = \delta_{lk}/f$ where $\delta_{lk} = 1$ if node l (or its symmetric equivalent) is a vertex of an element k; and $\delta_{lk} = 0$ otherwise. The coefficient f represents the number of elements with node l (or symmetric equivalent) as one of its vertices. After obtaining ODF $\boldsymbol{A}^{node}$, it has been sampled to the PF microstructure.

4.1. Identification of slip system parameters for different Ti-Al alloys

In this work, we have studied ODF modeling for tensile and compressive behavior of both HCP Ti-Al alloys (i.e., Ti-0Al and Ti-7Al) utilizing the CP model. In general, HCP α-Ti crystal structure predominately displays easy $\langle a \rangle$ slip, either on the basal or prismatic plane [93–95]. In pure HCP-Ti, the three main observed slip systems include three equivalent basal $0001\langle 11\bar{2}0 \rangle$, three equivalent prismatic $10\bar{1}0\langle 11\bar{2}0 \rangle$, and six equivalent pyramidal $10\bar{1}1\langle 11\bar{2}0 \rangle$ slip systems [93,94]. The aforementioned slip systems share a common $\langle 11\bar{2}0 \rangle$ or $\langle a \rangle$ slip direction. This slip has been denoted as $\langle a \rangle$-slip on basal, prismatic, and pyramidal slip systems. In the HCP system, other slip modes such as slips on pyramidal planes with $\langle 11\bar{2}3 \rangle$ or $\langle c+a \rangle$ slip or twinning deformation modes are required to accommodate strain parallel to c-axis. Additionally, twinning is commonly observed in HCP-Ti which has a strong influence on the overall deformation behavior of a polycrystal [94].

The deformation behavior of HCP-Ti and Ti alloys have been well studied [44,93–99] which reveals that the Ti alloys have complex slip and twinning modes. Such complexities arise mostly due to the crystallographic nature of the α-phase and the presence of alloying elements such as Al [96]. The influence of Al can be significant due to the effect of Al on the twinning mechanism [93,96–99] where Al addition can effectively suppress twinning [93,96,97]. It has been observed that the frequency of twinning rapidly decreases when the Al content increases and the nucleation of compression twins in Ti-Al single can be difficult when Al content > 5% [96]. The twinning mechanism has been suppressed in Ti-Al alloy with 6wt % Al even at low temperature 100 K [98]. Whereas, some studies suggest that Al addition can increase the twinning effect up to some threshold value where further Al addition mechanism suppresses the twinning mechanism [95,99]. It has been found that twinning activity is maximum at around 7wt%Al and a further increase in Al reduced the twinning activity due to short-range ordering and formation of Ti-3Al in Ti-Al alloys [99]. It has been concluded that $10\bar{1}2\langle \bar{1}011 \rangle$ tensile twin provides a near 90^o rotation of the c-axis from a tensile to a compressive stress condition, and increases the intensity of basal texture during compression. Additionally, EBSD data indicates that there is an increasing fraction of $10\bar{1}2\langle \bar{1}011 \rangle$ twins until 7 at.%Al, with further Al addition, it decreases. As a secondary twinning mode 4% of $11\bar{2}2\langle 11\bar{2}\bar{3} \rangle$ compression twins have been observed only in Ti-0Al. When modeling the Ti-Al alloys, the present study only considers the $10\bar{1}2\langle \bar{1}011 \rangle$ twin mechanism neglecting the small effect of the secondary twinning mode. Different slip system parameters of Ti-0Al and Ti-7Al have been identified through the CP model with ODF from experimental stress–strain data (see Section 6.1).

5. Phase field approach for simulating SRX and grain growth

During post-deformation annealing, polycrystalline material can undergo a drastic change in its microstructure through SRX and grain growth [3,4]. In general, grain growth phenomena are driven by the reduction of total grain boundary energy. Whereas, the SRX process is driven by the reduction of stored energy from dislocations [3,4]. To provide a realistic distribution of stored energy, the spatial distribution of dislocation density of plastically deformed microstructure before the annealing phase has been obtained from the CP model which is used as input for the stored energy. Subsequently, SRX and grain growth in a deformed microstructure have been simulated utilizing the PF model combined with CP-informed dislocation density.

5.1. Phase field model

Consider an initial configuration of a polycrystal Ω bounded in the domain $\Omega \subset \mathbb{R}^3$ with boundary $\Gamma \subset \mathbb{R}^2$, the different grain orientations of polycrystalline microstructure can be represented by a finite set of non-conserved order parameters $\hat{\xi} := (\xi_1, \xi_2, \ldots \xi_k, \ldots \xi_N)$. Here, the order parameter $\xi_k(\mathbf{X}, t)$ is a continuous function of spatial coordinate $\mathbf{X}$ and time t that independently represents the orientation of the k^{th}-grain; N is the total number of grains in the initial matrix phase of the polycrystalline microstructure. In the PF formulation, the proposed free-energy functional Ψ can be expressed as [68,69]:

$$\Psi = \int_{\Omega} (\psi^l + \psi^{\nabla}) \, d\Omega; \quad \psi^l = \breve{\psi} + \hat{\psi} \tag{8}$$

where total energy density ψ consists of local energy ψ^l and gradient energy ψ^{∇}; ψ^l is the sum of bulk energy $\breve{\psi}$ and stored energy $\hat{\psi}$. The bulk energy density $\breve{\psi}$ provides the driving force for grain growth is given as [76,77]:

$$\breve{\psi} = m_0 \left[-\frac{1}{4} \sum_{k=1}^{N} \xi_k^2 \left(2 - \xi_k^2\right) + \alpha \sum_{k=1}^{N} \sum_{l>k}^{N} \xi_k^2 \xi_l^2 + \frac{1}{4} \right]. \tag{9}$$

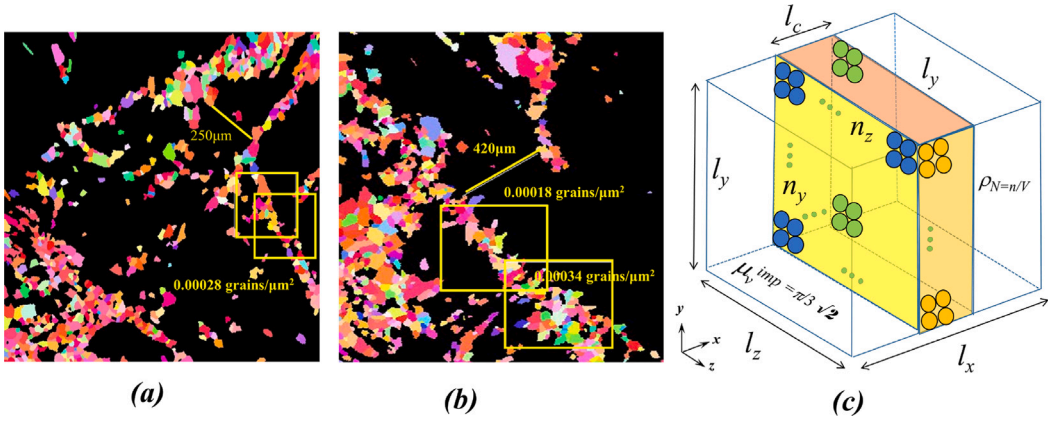

Fig. 6. (a, b) Experimental EBSD inverse pole figure image (IPF) showing the emergence of band-shaped clustering in two different partially recrystallized Ti-7Al samples where the yellow box are the representative areas used to measure nuclei density (ρ_N) along clustered bands; (c) schematic of RVE during complete impingement condition. (For interpretation of the references to colour in this figure legend, the reader is referred to the web version of this article.)

where the constant $m_0 \subset \mathbb{R}^+$ is the bulk energy density coefficient that depends on grain boundary energy and width; the PF model parameter $\alpha = 1.5$ can be chosen to impose symmetric distribution of $\xi_k(\mathbf{X}, t)$ across the interface Γ_{int}.

The term $\hat{\psi}$ in Eq. (8) represents the stored energy density in the plastically deformed grains accounting for dislocation accumulation which provides the driving force for microstructural evolution. Thus, relatively large deformed grains have relatively large $\hat{\psi}$ due to the dislocation generated during the deformation process. For simplicity, let us assume that the spatial distribution of the dislocation density ρ_k is uniform within corresponding grain-k ($k \forall 1, 2, \ldots, N$), the effective spatial dislocation density ρ_e for an arbitrary number of grains in the microstructure can be approximated from ξ_k and ρ_k with the following interpolation function [76,77] :

$$\rho_e(\xi_1, \xi_2, \ldots \xi_N) = \frac{\sum_{k=1}^{N} \xi_k^2 \rho_k}{\sum_{l=1}^{N} \xi_l^2}, \tag{10}$$

As previously mentioned, the CP model has been employed to obtain dislocation density ρ_i^{CP} (see Eq. (4) in Section 2) for grain i. Thus, the spatial distribution of stored energy density $\hat{\psi}$ takes the following form [100]:

$$\hat{\psi} = \frac{1}{2} G b^2 \rho_e^{\mathrm{CP}}(\xi_1, \xi_2, \ldots \xi_N) = \frac{1}{2} G b^2 \rho_e^{\mathrm{CP}}(\hat{\xi}_i) \tag{11}$$

where G and b are the shear modulus and Burgers vector of the dislocations, respectively. The gradient energy density ψ^{∇} allows one to control the diffuse interface width at the grain boundary which can be expressed as :

$$\psi^{\nabla} = \frac{\beta}{2} \sum_{k=1}^{N} |\nabla \xi_k|^2 \tag{12}$$

where β is the gradient energy coefficient. Finally, from ψ in the Eq. (8), time-dependent evolution equations for the nonconserved order parameters can be obtained from the Allen-Cahn dynamics [101] as:

$$\frac{1}{L} \frac{\partial \xi_k}{\partial t} = -\frac{\delta \Psi}{\delta \xi_k} = m_0 \left[\xi_k (1 - \xi_k^2) - 2\alpha \xi_k \sum_{l \neq k}^{N} \xi_l^2 \right] + \beta \nabla^2 \xi_k - G b^2 \frac{\xi_k}{\sum_{l=1}^{N} \xi_l^2} (\rho_i - \rho_e) \tag{13}$$

where $L \subset \mathbb{R}^+$ is the Allen-Cahn mobility.

5.1.1. Nucleation procedure

Experimental observations during SRX indicate that the nucleation is more favorable to occur on grain boundaries than sub-grain under uniform deformation [3]. Compared to the grain boundary, the triple grain boundary is energetically more favorable for nucleation due to the larger grain boundary area density [102]. Thus, in the current study, a probabilistic nucleation algorithm [69,103] has been adopted such that, during plastic deformation, the probability of nucleation of newly SRX grain is favorable in the grain boundary and triple grain boundary due to misfit strain. The relative probability $P(\mathbf{X})$ of forming nucleus at position $\mathbf{X}$ can be expressed as :

$$P(\mathbf{X}) = \left(\sum_{k}^{N} |\nabla \xi_k(\mathbf{X})| - min \sum_{k}^{N} |\nabla \xi_k(\mathbf{X})| \right) / \left(max \sum_{k}^{N} |\nabla \xi_k(\mathbf{X})| - min \sum_{k}^{N} |\nabla \xi_k(\mathbf{X})| \right) \tag{14}$$

where $\sum_k^N |\nabla \xi_k(\mathbf{X})|$ describes grain boundary morphology of the microstructure with $P(\mathbf{x}) \simeq 1$ on triple grain boundary, $0 < P(\mathbf{x}) < 1$ on grain boundary, and $P(\mathbf{x}) = 0$ inside the grains. Initially, spherical nuclei of diameter d_i with a diffused interface profile $\xi_k^n = 0.5 \left[1 - \tanh\left(\frac{d - 0.5 d_i}{2\Delta l}\right)\right]$ has been considered where d is the distance from position $\mathbf{X}$ to the center of the seeded nuclei; Δl is the grid spacing [69]. Due to the size difference between SRX nucleus size and the scale of microstructure, a relatively large seed size r_s has been selected. To compensate larger seed, a correction time t_{RX}^c has been introduced [69]. From the Bailey-Hirsch criterion, the critical radius size r_{BH} corresponding to the maximum change in free energy can be expressed as :

$$r_{BH} = \frac{(n_{dim} - 1)\gamma_{gb}}{\bar{f}_s} = \frac{2(n_{dim} - 1)\gamma_{gb}}{\bar{\rho} G b^2} \tag{15}$$

where $n_{dim} = 3$ is for three dimensions; γ_{gb} is the grain boundary energy; $\bar{f}_s$ and $\bar{\rho}$ are average stored energy and average dislocation density, respectively. Furthermore, the seed growth time t_s can be defined as : $t_s = (r_s - r_{BH})/V_{gb}$, where V_{gb} is the growth velocity of the nuclei. Finally, the stabilization of nuclei can be ensured by incorporating initial hold time, $t_h = 200\Delta t$ resulting in corrected recrystallization time, $t_{RX}^c = t_n + t_s - t_h$, where t_n is the nominal simulation time (more details can be found in [69]). This PF model simulates static recrystallization by inserting spherical, dislocation-free nuclei into the computational domain at the start of the simulation [68,69]. The evolution equations in Eq. (13) have been solved numerically using the finite difference method on a uniform three-dimensional grid utilizing forward Euler time stepping. Due to the presence of large amounts of grains in the microstructure, the simulations are computationally challenging. Thus, active parameter tracking is utilized to efficiently simulate the microstructure. Order parameters are only stored for positions where $\xi_k(x, y, z) > 1 \times 10^{-6}$ [104,105]. The data structure and algorithm are based on [106] extending it to simulate recrystallization with stored energy. The algorithm has been parallelized using the Message Passing

Interface (MPI). The PF parameters that have been used to simulate SRX in Ti-0Al and Ti-7Al have been detailed in Section 6.6.1.

5.2. Nuclei clustering during SRX

The experimental EBSD images of partially recrystallized microstructures of Ti-alloys (in particular Ti-7Al) reveal that, in many cases, the recrystallized samples contained bands of clustered SRX grains [87] indicating the existence of initial bands of clustered nuclei as shown in Fig. 6-(a, b). Such non-homogeneous distribution of SRX nuclei (or grains) does not conform to Avirami-type growth kinetics [107, 108] that follows uniform impingement condition (i.e., random nucleation) [109,110]. Therefore, it is important to study the influence of the spatial distribution of nuclei on the SRX microstructure and validate experimentally observed kinetics of SRX in the Ti-alloys. To address this, in the present study, we consider two different arrangements of SRX nuclei arrangements.

In the first arrangement, nuclei are placed randomly in the microstructural and we call it as *randomly distributed nuclei*. In a separate arrangement, following the experimental evidence, a banded distribution of nuclei is considered, and we name it *banded zone of nuclei* where nuclei are located within a vertical band that has a finite thickness but extends infinitely in two directions. The PF simulations based on these initial distributed of nuclei have been studied to examine how the spatial distribution of nuclei affects the evolution of the microstructure, the kinetics of SRX, and microstructural path descriptors (see Sections 6.7 and 6.8 for Ti-0Al and Ti-7Al, respectively).

5.3. Geometric impingement condition during SRX

In this section, a geometric theory has been formulated to predict the phenomenon of impingement of dislocation-free SRX grains during recrystallization for *banded zone of nuclei* cases to mimic the experimental observations. The goal is to quantify the geometric impingement properties during SRX, in particular, the average impingement diameter $d^{\,t}_{imp}$ and the volume fraction of recrystallization $(R_x^{imp})^t$ at impingement condition. Due to the heterogeneity of spatial distribution of dislocation density, the grain morphology of the newly recrystallized grains can be irregular which introduces complexity in the formulation. Thus, for simplicity, we assume homogeneous dislocation density that leads to isotropic growth of the SRX grain (i.e. perfect sphere) which is distributed uniformly in the confined layer of the cluster as the array of evenly spaced grains with diameter d.

Let us assume, the cross-section area of the sample RVE along yz-plane be $A_{yz} := l_y l_z$; where l_y and l_z are the lengths along y and z directions, respectively as shown in Fig. 6-(c). To make this theory purely geometrical, we further assume *complete impingement* will occur when the evenly spaced spherical grain simultaneously satisfies the following constraints: $l_y = n_y d_{imp}$ and $l_z = n_z d_{imp}$ at impingement condition; where n_y and n_z are a number of grains along y and z directions, respectively; total number of grains $n := n_y n_z = l_y l_z / d^2_{imp} = A_{yz}/d^2_{imp}$; volume of each grain $V_g = \frac{1}{6}\pi d^3_{imp}$. Now, we can define the nuclei density (i.e., number of nuclei per unit volume of deformed RVE) $\rho_N := n/V$ and volume fraction $R_x := \sum V_n / V$ where $\sum V_n := nV_g = \frac{1}{6} n\pi d^3_{imp}$ at *complete impingement* condition assuming maximum closed pack density at impingement as $\mu_v^{imp} = \pi/3\sqrt{2}$. From such definition, $d^{\,t}_{imp}$ and $(R_x^{imp})^t$ can be expressed as:

$$d^{\,t}_{imp} = 2\sqrt{\mu_v^{imp}/\pi\rho_N\, l_c} \qquad (R_x^{imp})^t = \frac{\pi}{6} d^{\,3}_{imp} \tag{16}$$

where l_c is the specimen length orthogonal to the impingement plane. In the formulation, a single layer of grains along the xy plane is considered. Since, for the case of multiple layers, once nuclei impinge on each other at different layers, they are unable to expand freely. Therefore, after impingement, the transition from 3D grain growth to 1D grain growth occurs which ensures the complete impingement along the yz plane.

5.4. Nuclei density

During SRX, the initial number density of nuclei, N_{REX} can be obtained assuming that all seeded nuclei persist. Using experimental microstructures, N_{REX} can be approximated using the following expression [111]:

$$N_{REX} = \left[\frac{4}{3}\pi\left(\frac{D_{REX}}{2}\right)\right]^{-1} \tag{17}$$

where D_{REX} is the average grain size at the completion of SRX. The number of nuclei N_t can be determined from N_{REX} and V as $N_t = N_{REX}\, V$. For *randomly distributed nuclei*, nuclei are stochastically inserted into the RVE as described in [69]. To realistically simulate clustering during SRX, information from partially recrystallized EBSD scans was used as shown in Fig. 6-(a, b). The density of SRX grains in each of the representative areas (i.e., yellow boxes in Fig. 6) are considered and the average of these regions has been used to take into account for sample variability (see Section 6.6.1). From the experimental characterization, newly SRX grains are placed only within the midsection of the sample RVE transverse to the loading direction to mimic the *banded zone of nuclei* configuration. This region has a thickness of $l_c = 0.125l$, where l is the sample size.

6. Results and discussions

6.1. Optimized slip system parameters for different Ti-Al alloys

In the present study, different slip system parameters of Ti-0Al and Ti-7Al are calibrated by solving an inverse optimization problem using the CP model. The Non-Dominated Sorting Genetic Algorithm (NSGA-II) [112] is utilized as the optimization method to calibrate the CP model against the experimental stress–strain data. The optimization is performed to identify the design variables for 5 different slip systems considered for the SRX process. These slip systems include the basal $\langle a\rangle$, prismatic $\langle a\rangle$, pyramidal $\langle a\rangle$, and pyramidal $\langle c+a\rangle$ in addition to the $10\bar{1}2\langle\bar{1}011\rangle$ twinning mechanism. A total of 20 design variables including 4 different slip system parameters (i.e., s_0, h_0, s_s, and a) are calibrated for the aforementioned slip and twin systems. The objective function is defined as the minimization of the L_2 norm error between the CP predictions and experimental data for true strain-true stress curves. The lower bounds of the optimization variables (slip system parameters for basal $\langle a\rangle$, prismatic $\langle a\rangle$, pyramidal $\langle a\rangle$, pyramidal $\langle c+a\rangle$ slip systems and twinning) are obtained using the available information in [113]. A random initial texture distribution is assumed for all cases. Mathematically, the optimization problem can be formulated as:

$$min \quad \epsilon \tag{18}$$

$$s = (s_0, h_0, s_s, a) \tag{19}$$

In Eq. (18), ϵ represents the L_2 norm error between strain-stress curves from the experimental observation and CP simulation. In Eq. (19), s is the vector of optimization variables. A quadratic interpolation is implemented to match the experimental and computational strain points. In the computations, the strain rate is defined as 2.5×10^{-4} and the simulations are performed until the last available experimental strain data point. Finally, the optimization problem is solved by utilizing NSGA-II combined with a global sampling strategy, Incremental Space Filler (ISF) [114], in Modefrontier software. The CP simulations are performed to investigate compression and tensile stress–strain behavior of both Ti-0Al and Ti-7Al. The elastic parameters are taken from [115] as: $C_{11} = C_{22} = 175$ GPa, $C_{12} = 88.7$ GPa, $C_{13} = C_{23} = 62.3$ GPa, $C_{44} = C_{55} = 62.2$ GPa, and $C_{66} = (C_{11} - C_{12})/2$.

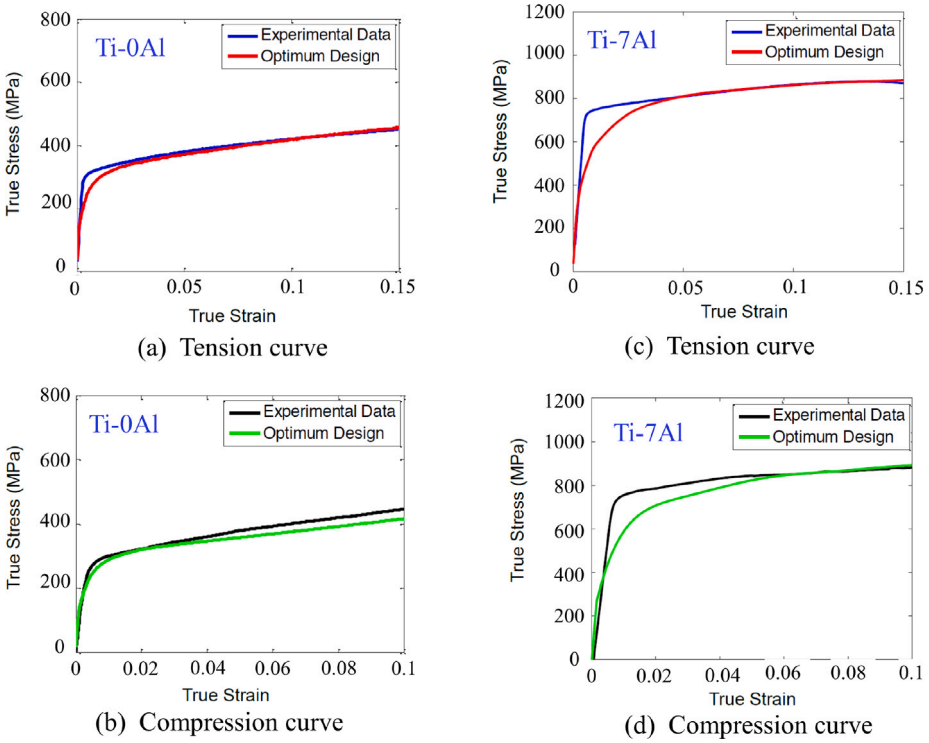

Fig. 7. Comparison between uniaxial true strain-true stress curves from experimental data and optimum design for (a, b) Ti-0Al; (c, d) Ti-7Al. All stress values are in MPa.

Table 1
Optimized slip and twin resistance and hardening parameters from CP simulation calibrated using the experimental stress–strain curves for Ti-0Al alloy.

Slip system	s_0	h_0	s_s	a
Basal $< a >$	88.10 MPa	215.60 MPa	1175.90 MPa	0.25
Prismatic $< a >$	89.50 MPa	215.60 MPa	1175.90 MPa	0.25
Pyramidal $< a >$	161.10 MPa	215.60 MPa	1175.90 MPa	0.25
Pyramidal $< c + a >$	355.20 MPa	215.60 MPa	1175.90 MPa	0.25
Twinning $< c + a >$	507.70 MPa	200.10 MPa	1175.90 MPa	0.25

Table 2
Optimized slip and twin resistance and hardening parameters from CP simulation calibrated using the experimental stress–strain curves for Ti-7Al alloy.

Slip system	s_0 (MPa)	h_0 (MPa)	s_s (MPa)	a
Basal $< a >$	215.51 MPa	216.18 MPa	1534.20 MPa	1.38
Prismatic $< a >$	250.00 MPa	216.18 MPa	1534.20 MPa	1.38
Pyramidal $< a >$	991.40 MPa	216.18 MPa	1534.20 MPa	1.38
Pyramidal $< c + a >$	999.30 MPa	216.18 MPa	1534.20 MPa	1.38
Twinning $< c + a >$	783.37 MPa	1049.70 MPa	1534.20 MPa	3.96

6.1.1. Optimized slip system parameters for Ti-0Al

For Ti-0Al, the optimum slip system parameters are shown in Table 1. The optimization results for Ti-0Al indicate that s_0 of pyramidal $\langle c + a \rangle$ slip system is 3 to 5 times higher than s_0 of prismatic $\langle a \rangle$ slip system which is similar to the suggested value for Ti-0Al [95]. Using the optimum design parameters, the predicted true stress-true strain curves from the ODF-based CP model for both tension and compression curves are compared with the experimental observations in Fig. 7-(a) and Fig. 7-(b), respectively. The comparison illustrates that the optimum slip and twin system parameters can efficiently reproduce the tension and compression test data for Ti-0Al.

6.1.2. Optimized slip system parameters for Ti-7Al

The optimum slip and twin system parameters of Ti-7Al are reported in Table 2. These optimum parameters are also compared to the critical resolved shear stress (CRSS) values of different slip systems from existing literature for Ti-7Al. It is observed that the optimum CRSS value obtained from our CP-PF-SRX model is in excellent agreement with the previous results [93,95,96]. In addition, the CRSS values of twinning and pyramidal $\langle a \rangle$ slip system have also been identified. The tensile and compressive curves obtained through the CP simulation using the optimum design parameters are compared with the experimental curves as depicted in Figs. 7 -(c, d).

Overall, the optimized slip and twin system parameters can generate a reasonably well computational representation of the experimental tension and compression data. The optimum results for both Ti-0Al and Ti-7Al provide a satisfactory resemblance with the experimental data. However, the difference between the experimental and computational models can be attributed to the uncertainty of the initial texture [43,45–50]. The ODF-based CPFE simulations are performed by assuming a randomly oriented initial crystallographic texture, however, in reality, the experimental texture slightly varies from the random texture and corresponds to a weakly basal texture. Nevertheless, the CP model can still identify the optimum parameters under the effect of initial texture uncertainty for relatively low strain values. It is noteworthy to mention, a better calibration of optimized slip and twin system parameters for Ti-7Al could be found in [47,116].

6.2. Initial representative volume element for SRX

In the present study, a 3D polycrystalline microstructure obtained from the PF model has been considered as the initial representative volume element (RVE) as shown in Fig. 8-(a, b). The RVE is then used as an input in the CP model to obtain spatial distributions of dislocation density in the grains which have been used to simulate SRX and grain growth in the PF model for both Ti-0Al and Ti-7Al alloys. In the PF model, the initial RVE has been constructed by randomly seeded nuclei into the empty simulation domain (without any order parameters). These seeded nuclei are then evolved without stored energy until the simulation domain has been filed with grains [69,106]. The initial RVE polycrystal contains 750 grains with an average grain size of $50.2\Delta x =$

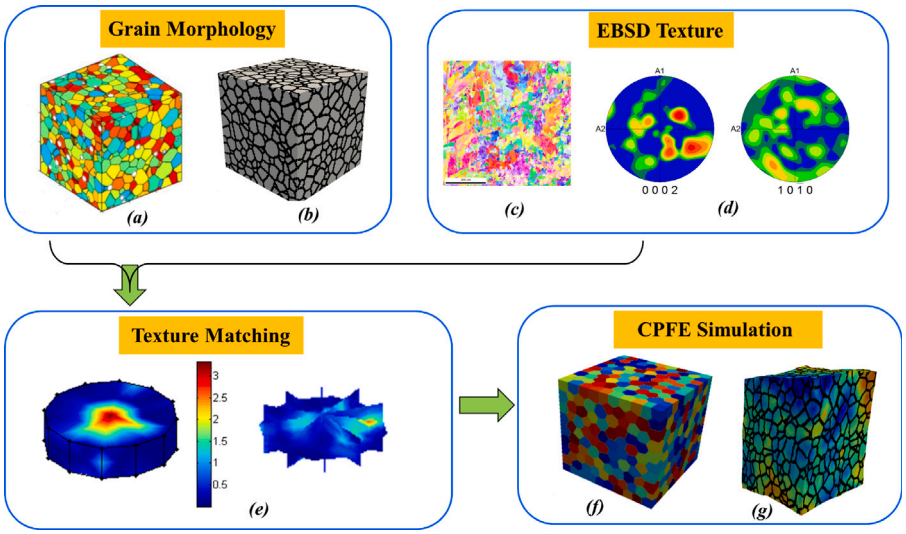

Fig. 8. Workflow for creating initial Representative Volume Element (RVE) considered for simulating SRX where (a, b) initial grain morphology from PF model with (c, d) EBSD grain orientation and pole figures data used for (e) texture matching algorithm to obtain (f, g) relative dislocation densities distribution in undeformed and deformed RVE from CP model.

25.1 μm on a 600 × 600 × 600 uniform grid (i.e. 300 μm×300 μm×300 μm simulation domain) as shown Fig. 8-(a). The average grain size can be obtained from the Eq. (17) for a given initial number density of nuclei which has been obtained from experimental characterization as shown in Figs. 6-(a,b). As detailed in Section 6.4, an efficient initial texture-matching procedure has been performed from the experimental EBSD and grain orientation data as shown in Fig. 8-(c, d). Noteworthy to mention, a relatively large number of grains in the aforementioned RVE ensures a more accurate representation of the experimental texture of Ti-alloys [117,118]. Along with the optimized slip system parameter obtained from ODF simulation, CP was then performed to obtain relative dislocation densities ρ_e^{CP} for each grain in the initial microstructure that was plastically compressed to 20% at ambient temperature (see additional discussion in Section 6.5).

6.3. Initial texture-matching procedure from experimental EBSD data

Before the deformation process, an efficient initial texture matching procedure has been employed to accurately represent the experimental EBSD texture of Ti-alloys into initial RVE. Once the ODF is obtained, the texture matching algorithm [118,119] has been utilized to match to RVE polycrystalline microstructure. The orientations of independent nodes have been assigned to the individual grains of the microstructure and the ODF ($\boldsymbol{A}^{node}$) is then matched to the RVE. The ODF values ($\boldsymbol{q}_i\boldsymbol{A}_i$) are multiplied by the number of grains (N_g) [118,119]. Each ODF can be represented as $N\boldsymbol{q}_i\boldsymbol{A}_i$ which approximates the number of grains constituting that orientation. We then split each value of $N\boldsymbol{q}_i\boldsymbol{A}_i$ by dividing it into equal parts (P_i) with its rounded number (e.g., 4.2 split into 4 parts of 1.05 each). In the present study, the range of the obtained P_i is 0.6–1.4. These numbers for the different grains can be directly matched to their respective relative grain volumes (defined as $N_gV_i/(\Sigma_iV_i)$ where N_g is the number of grains; V_i is the volume of each grain). Larger grains get assigned to orientations corresponding to grains with larger P_i values. Better representative matching can be ensured by increasing the number of grains. It is noteworthy to mention that the initial and under-compression experimental pole figures have been obtained from different samples. The boundary conditions for the RVE used in the CPFE simulation are $u_x = 0$ on $x = 0$, $u_y = 0$ on $y = 0$, $u_z = 0$ on $z = 0$. During compression, $u_z = -0.2$ has been prescribed on $z = 1$. The initial RVE has been matched to the weakly basal initial experimental microstructure. In the PRISMS plasticity CPFE simulation, twin systems have been initially considered as slip systems and are sheared until they are reoriented [90]. Since the initial texture in the experimental sample is weakly basal in nature and twin extension systems are generally less active in ND compression (i.e., z-direction compression as shown in Fig. 11). Thus, the twin reorientation has been ignored for our CPFE simulation.

6.4. Comparison of CP pole figures with experiments

The comparison between the texture of the parent sample and initial RVE microstructure in terms of {0002}, {10$\bar{1}$0}, and {10$\bar{1}$1} pole figures at $\varepsilon_{xx} = 0\%$ has been shown in Figs. 9(a, b) and 10(a, b) for Ti-0Al and Ti-7Al, respectively. The initial pole figures for the RVEs as computed by the texture matching algorithm indicate that the pole figures of the RVEs match accurately with the initial microstructure from the experiment for both Ti-alloys. On the other hand, Figs. 9(c, d) and 10(c, d) show the comparison of textures at $\varepsilon_{xx} = 20\%$ between experimentally observed textures and CP prediction for Ti-0Al and Ti-7Al, respectively. Under compression, Ti-0Al and Ti-7Al alloys have their $\langle c\rangle$ axis realigned in the compression direction. To emphasize model prediction, Figs. 9-(d) and 10-(d) shows $\langle c\rangle$ axis moving to the TD poles under compression along TD which is the primary mechanism for twinning activation. For Ti-7Al, there is an experimental mismatch between the initial sample and the one used for compression. The CPFE simulations indicate that it would align away from the $\langle c\rangle$ axis for the given initial microstructure as is shown in Fig. 9-(d). Nevertheless, the overall comparisons show that the pole figures capture the expected features of the simulated sample by correctly identifying compression poles during plastic deformation at room temperature as depicted in Figs. 9–10.

6.5. Evolution of dislocation density, stress and strain during plastic deformation

The evolution of the spatial distribution of relative dislocation density in RVE for Ti-0Al has been shown in Figs. 11 -(a, b, c) for various intermediate strain values. As it is to be observed that Ti-0Al is strongly basal as can be seen in the pole figure in Fig. 9 compared to Ti-7Al (see Fig. 10), hence the evolution of dislocation density shows that Ti-7Al relative dislocation density reaches a distribution with a relatively large number of grain which is closer to relative dislocation density value of one as shown in Figs. 11 -(a, b, c), followed by Ti-0Al. This is because the $\langle c + a\rangle$ pyramidal slip systems get activated at a lower strain level

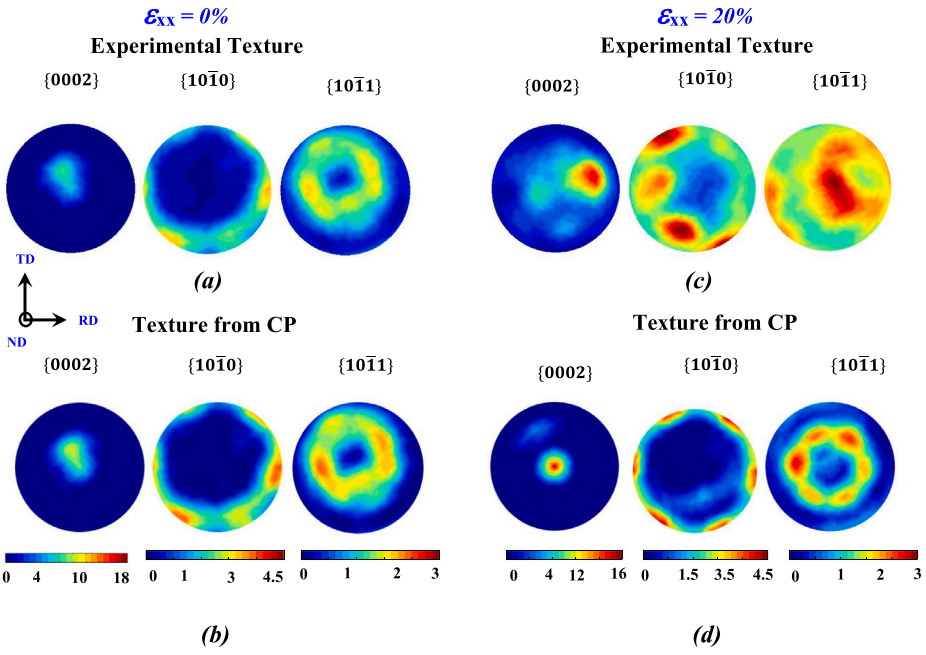

Fig. 9. Comparison of {0002}, {10$\bar{1}$0}, and {10$\bar{1}$1} pole figures for initial texture between (a) parent sample at ambient temperature and (b) initial RVE microstructure with texture initialized into the CP input model before deformation; final texture between (c) experimental EBSD microstructure and (d) predicted texture from CP simulation after deformation at compressive strain $\varepsilon_{xx} = 20\%$ for Ti-0Al.

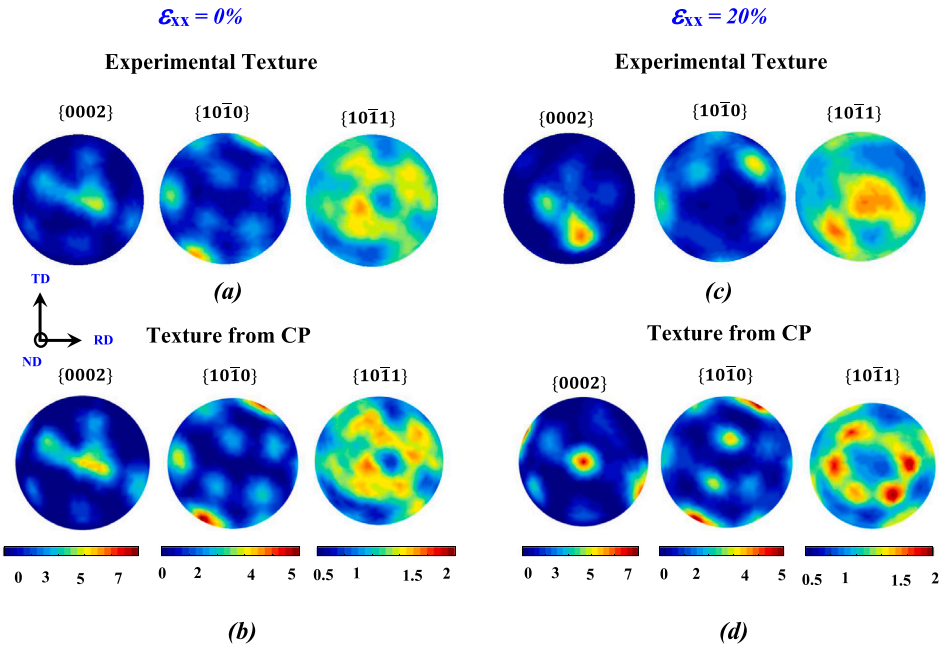

Fig. 10. Comparison of {0002}, {10$\bar{1}$0}, and {10$\bar{1}$1} pole figures for initial texture between (a) parent sample at ambient temperature and (b) initial RVE microstructure with texture initialized into the CP input model before deformation; final texture between (c) experimental EBSD microstructure and (d) predicted texture from CP simulation after deformation at compressive strain $\varepsilon_{xx} = 20\%$ for Ti-7Al.

in Ti-7Al as compared to Ti-0Al. As the $\langle c \rangle$ slip systems get activated, all the grains enter the plastic deformation regime and eventually the distribution will get tighter close to 1 for the majority of the grains. To further illustrate this point, in addition, N_g vs. ρ/ρ_{ave} obtained from CPFE simulation for intermediate ε_{xx} have been shown in Figs. 11-(d, e, f) and 13-(d, e, f) for Ti-0Al and Ti-7Al, respectively. The exponential distribution indicates that fewer grains are plastically deformed and the remainder of the grains remain in an elastic regime. Slowly, as the strain increases, more grains start getting plastic deformation and the distribution gets even with more grains closer to the average dislocation density.

The evolution of Lagrangian strain (E_{XX}) and Von Mises stress (σ_v) for Ti-0Al and Ti-7Al have been shown in Fig. 12 and Fig. 14, respectively for different strain values. Similar to the distribution of relative dislocation density, it is to be seen that the Lagrangian strain and Von Mises are more evenly distributed in Ti-7Al as compared to Ti-0Al. The underlying mechanism is the same in that $\langle c+a \rangle$ pyramidal slip

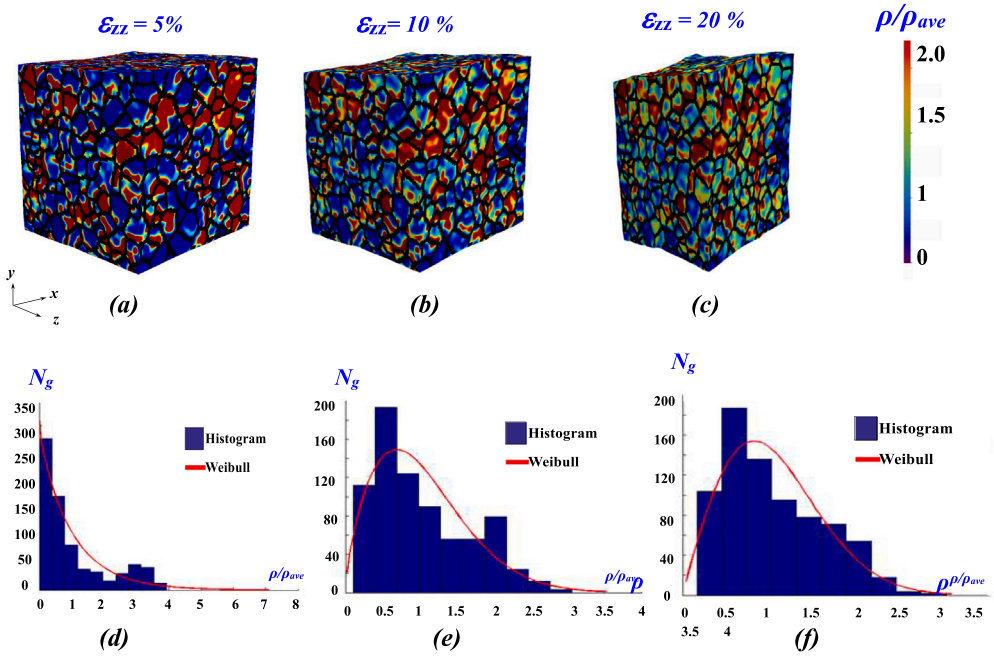

Fig. 11. Evolution of (a-c) spatial distribution of relative dislocation density (ρ/ρ_{ave}) in RVE and corresponding (d-f) N_g vs. ρ/ρ_{ave} curves obtained from CPFE simulation at (a, d) $\epsilon_{xx} = 5\%$, (b, e) $\epsilon_{xx} = 10\%$, and (c, f) $\epsilon_{xx} = 20\%$, respectively for Ti-0Al.

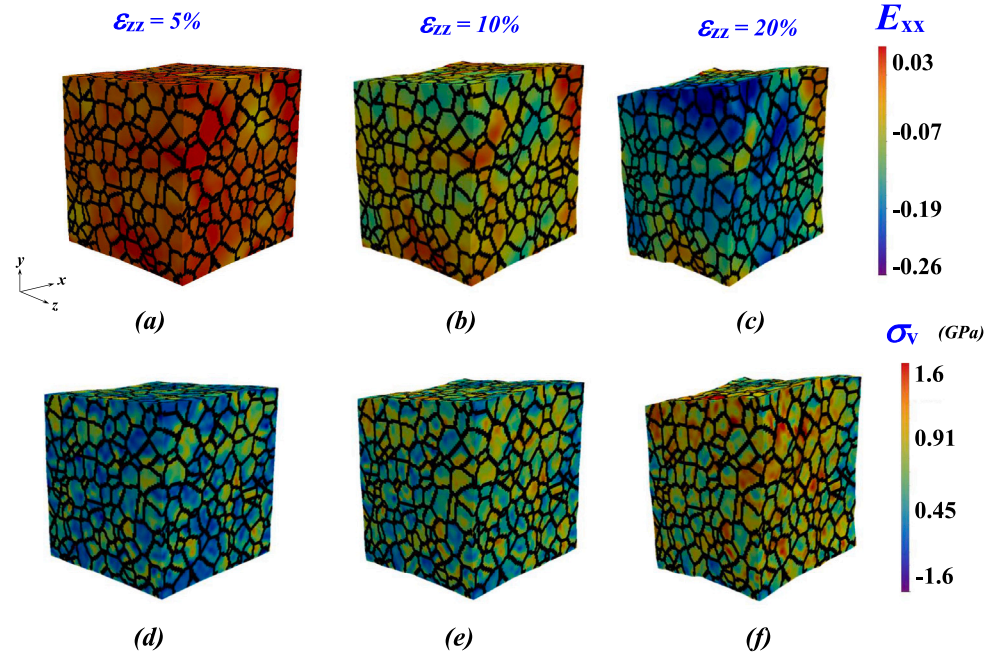

Fig. 12. Evolution of (a-c) Lagrangian strain component E_{xx}; (d-f) corresponding von mises stress σ_v obtained from CPFE simulation at (a, d) $\epsilon_{xx} = 5\%$, (b, e) $\epsilon_{xx} = 10\%$, and (c, f) $\epsilon_{xx} = 20\%$, respectively for Ti-0Al. All the stress values are in GPa.

systems get activated at a lower strain level in Ti-7Al as compared to Ti-0Al. In addition, Ti-7Al has a higher average von Mises stress followed by Ti-0Al. The reason can be attributed to the higher hardening values as is seen in the stress–strain curve for Ti-7Al compared to Ti-0Al (see Fig. 7).

6.6. Microstructural evolution during SRX for Ti-0Al and Ti-7Al

Next, during the annealing phase at 800 °C, the PF model has been used to simulate SRX and grain growth in Ti-alloys. The initial polycrystalline RVE sample has been compressed to 20% along the x-axis at room temperature and the corresponding spatial distribution of ρ_e^{CP} has been obtained from the CP simulation which is inputted into PF model to simulate SRX for both Ti-0Al and Ti-7Al alloys.

6.6.1. CP-PF-SRX model parameters

For simulating SRX, non-dimensional PF simulations have been performed with the following material parameters for Ti-alloys: $\beta = 2$, $L = 1$, $\alpha = 1.5$, $m_0 = 1$, $G = 2.5$, and b=1 [69]. A non-dimensional grid size, Δx=1, has been used for all simulations. The initial RVE

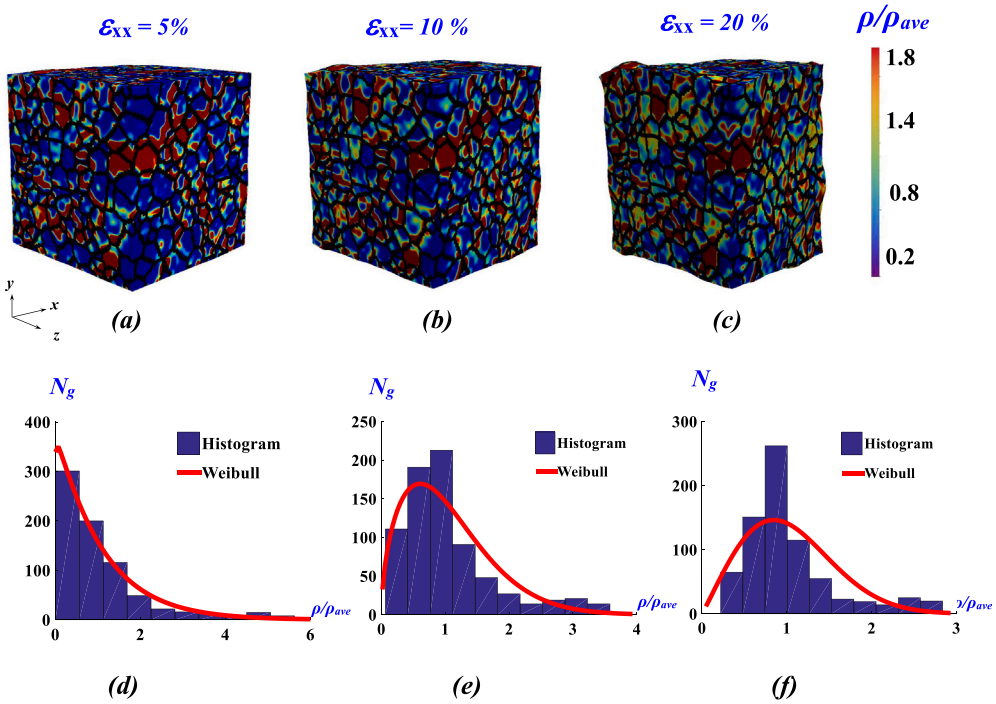

Fig. 13. Evolution of (a-c) spatial distribution of relative dislocation density (ρ/ρ_{ave}) in RVE and corresponding (d-f) N_g vs. ρ/ρ_{ave} curves obtained from CPFE simulation at (a, d) $\epsilon_{xx} = 5\%$, (b, e) $\epsilon_{xx} = 10\%$, and (c, f) $\epsilon_{xx} = 20\%$, respectively for Ti-7Al.

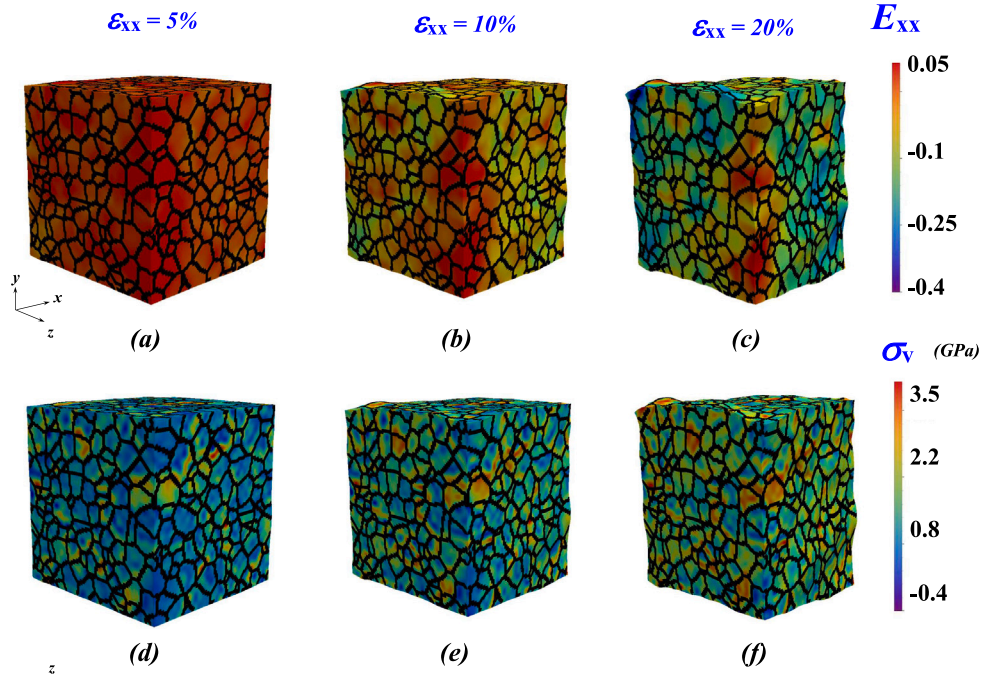

Fig. 14. Evolution of (a-c) Lagrangian strain component E_{xx}; (d-f) corresponding von mises stress σ_v obtained from CPFE simulation at (a, d) $\epsilon_{xx} = 5\%$, (b, e) $\epsilon_{xx} = 10\%$, and (c, f) $\epsilon_{xx} = 20\%$, respectively for Ti-7Al. All the stress values are in GPa.

microstructure has 750 grains with an average grain size of $50.7\Delta x$ on a $600 \times 600 \times 600$ uniform grid (see details in Section 6.2). Following CP, PF parameters are collected from literature as grain boundary energy 0.7 J/m^3 [87]; grain boundary mobility 5.0×10^{-11} m^4/J-s at 800 °C [87]; shear modulus $G = 42$ GPa for α-Ti [93]; burgers vector $b = 0.295$ nm for an $\vec{a}$ dislocation in Ti [120] and stored energy constant $C = 0.15$ [111]. For Ti-0Al, following parameters have been considered: Taylor factor M_T =5.30 [121]; yield stress σ_y = 324 MPa [87]; flow stress σ = 717.6 MPa at ϵ = 20% that results in $\rho_{ave} = 1.51 \times 10^{15}$/ m^2 from Eq. (3). Whereas, for Ti-7Al, we take M_T =4.82 [121]; σ_y = 629 MPa [122]; σ = 1227.01 MPa at ϵ = 20% to get $\rho_{ave} = 4.23 \times 10^{15}$/ m^2 For the SRX simulations, considering initial nuclei density

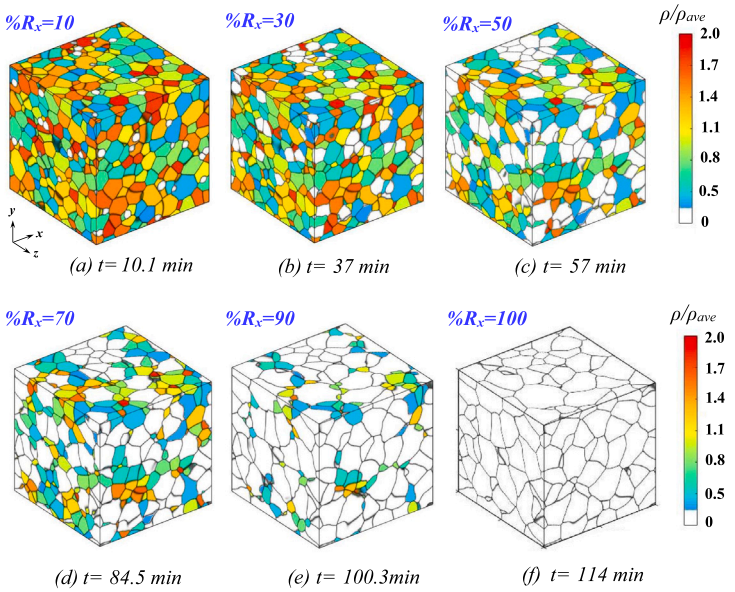

Fig. 15. Microstructural evolution in Ti-0Al during SRX at 800 °C for R_x: (a) 10%; (b) 30%; (c) 50%; (d) 70%; (e) 90%; (f) 100% in deformed ($\varepsilon_{xx} = 20\%$) RVE cubic sample for random nuclei distribution sites with CP-informed ρ/ρ_{ave}.

$\rho_N = 5.5 \times 10^{12}$ m^{-3} from experimental characterization [87] results in $N_t = 149$ that have been considered for both of nuclei arrangements. All simulations are conducted using periodic boundary conditions. The simulations are performed with uniform domain decomposition, utilizing MPI parallelization in high-performance computing resources.

6.6.2. Microstructural evolution for random nuclei

In the first case, initial nuclei are assigned randomly based on probabilistic nucleation criteria (see Section 5.1.1) and corresponding time evolution of SRX microstructure for intermediate values of $\%R_X$ have been shown in Figs. 15 and 16 for Ti-0Al and Ti-7Al, respectively. Fully recrystallized grains are shown in white with $\rho/\rho_{ave} = 0$. The nucleation is found to occur at sites of high strain, mostly corresponding to the regions near the grain boundaries (see Figs. 15-b or 16-b for example). These grains then start to grow at relatively high plastic strain (i.e., high stored energy) and spread into the low plastic strained region over time. Initial growth of SRX grains is seen to be quite rapid until finally coalesce locally (see Figs. 15-d or 16-d). On the other hand, relatively slow evolution occurs in the zone where the SRX grains are absent. The RVE microstructure is fully recrystallized (i.e., $\%R_X$=100) much faster for Ti-0Al with $t = 114$ min compared to Ti-7Al with $t = 566.4$ min for higher driving force due to relatively high ρ/ρ_{ave} distribution.

6.6.3. Microstructural evolution for banded nuclei

In our second scenario, as shown in Figs. 17 and 18 for Ti-0Al and Ti-7Al, respectively, we study SRX microstructural evolution under initial clustering of nuclei to simulate more realistic nucleation arrangement experimentally observed in the Ti-alloys. The thickness of the clustered nuclei band and nuclei density has been directly obtained from the experimental information from partially recrystallized EBSD scans (see Section 5.3). In our simulation, we consider a clustered nuclei band of thickness $l_c = 0.125\,l$ along the yz plane in polycrystalline RVE to study the effect of grain impingement on SRX microstructure. During the initial phase of microstructural evolution, significant grain growth is observed in the zone of seeded nuclei. Afterward, the preferential impingement occurs early in the SRX process. In other words, until the growing surfaces of recrystallized grains impinge each other, as shown in Fig. 17-(b) for Ti-0Al at $\%R_x^{imp} \simeq 30$, the transition from 3-D to 1-D grain growth eventuates. Due to grain impingement, the recrystallized grains evolve to grow unidirectionally with a larger aspect ratio along x-direction. Eventually, as shown in Figs. 17-(f) and 18-(f) for Ti-0Al and Ti-7Al, respectively, complete SRX will occur with the grains from a neighboring cluster as represented by periodic boundary conditions in the PF model.

6.7. The effect of microstructural heterogeneities on the SRX Kinetics for T-0Al

6.7.1. Avirami kinetics of SRX

The nucleation and growth kinetics of the SRX process in metals such as Ti-alloys, in general, can be described by the classical Avrami relationship [107,108] where the volume fraction of recrystallized grains (R_x) has been assumed to be a sigmoidal function of annealing time (t) in the form:

$$R_x = 1 - e^{-\lambda\left(\frac{t}{t_{0.5}}\right)^n} \tag{20}$$

where $\lambda = -\ln(0.5)$; $t_{0.5}$ is the time required to achieve $\%R_x = 50$, and Avrami exponent n is the dimension dependent time exponent. The Avrami transformation kinetic is based on the assumptions of the random spatial distribution of nuclei with constant nucleation rate and normal velocities of interfaces both in space and time until impingement with $n = 3$ is expected for growth in 3D [3,123]. For random nuclei case, as shown in Fig. 15, fitting the $\%R_x$ vs. t to Eq. (20) yielded an Avrami time exponent of $n = 2.89$ with $t_{0.5} = 57.00$ min for Ti-0Al which is in agreement with the expected value for site-saturated nucleation in 3D (i.e., $n \approx 3$). Thus, the results validate that the proposed CP-PF-SRX framework can predict Avrami-type kinetics in simulating SRX. To further examine a more complex case, we considered the kinetics of SRX with clustered nuclei in a planar region (as shown in Fig. 16) that results in $n = 1.17$ with $t_{0.5} = 83.20$ min for Ti-0Al. For the clustered band of nuclei, before impingement, growth can occur in all three directions. However, such rapid growth of the SRX grains has been restricted along yz-plan early in the SRX process (i.e., after impingement $\%R_x^{imp} \simeq 30$). Therefore, the growth rate of the SRX grains slows down and is no longer constant orthogonal to the preferential growth plane (i.e., yz-plan). For $\%R_x^{imp} \geq 30$, the growth dimension (i.e. x-direction) is still free and unaffected by the clustering. Such restricted mechanism of grain impingement leads to a decrease in Avrami exponent to $n \approx 1$ signifying 1D SRX

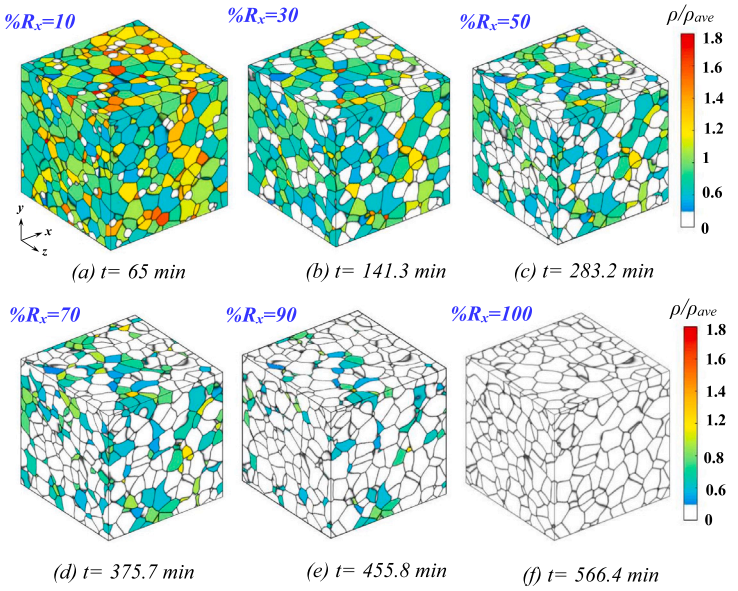

Fig. 16. Microstructural evolution in Ti-7Al during SRX at 800 °C for R_x: (a) 10%; (b) 30%; (c) 50%; (d) 70%; (e) 90%; (f) 100% in deformed ($\epsilon_{xx} = 20\%$) RVE cubic sample for random nuclei distribution sites with CP-informed ρ/ρ_{ave}.

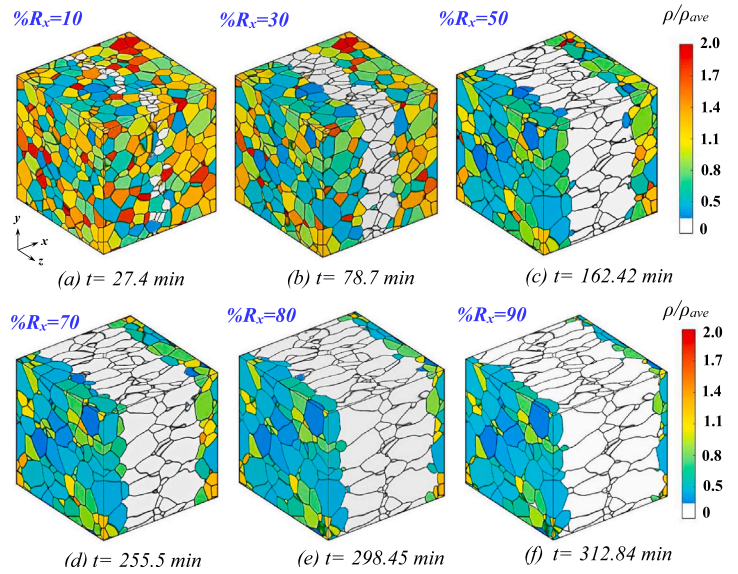

Fig. 17. Microstructural evolution in Ti-0Al during SRX at 800 °C for R_x: (a) 10%; (b) 30%; (c) 50%; (d) 70%; (e) 80%; (f) 90% in deformed ($\epsilon_{xx} = 20\%$) RVE cubic sample for banded nuclei distribution sites with CP-informed ρ/ρ_{ave}. SRX nuclei are positioned at the midsection of the x-axis, along the yz plane of a thickness of 1/8th of the sample size.

Table 3
Comparison of Avrami constants, $t_{0.5}$, R^2, S_V^{max}, $\%R_x^{S_v}$, d_{imp}^t, and $(R_x^{imp})^t$ for different cluster arrangements from CP-PF-SRX model and proposed impingement theory for Ti-0Al at 800 °C.

Cluster arrangement	n	$t_{0.5}$ (in min)	R^2	S_V^{max}	$\%R_x^{S_v}$	d_{imp}^t (in μm)	$\%(R_x^{imp})^t$
Random Nuclei	2.89	57.00	0.72	0.038	51.7	–	–
Banded Nuclei	1.17	83.20	0.91	0.036	32.52	48.82	37

growth. Noteworthy to mention, our result illustrates that the proposed framework can capture such heterogeneous grain impingement kinetics that is a significant deviation from the original Avirami-type kinetics for homogeneous growth of SRX.

6.7.2. Grain size distribution (GSD)

In order to shed light on the evolution of grain morphology for two different nuclei arrangements, grain size distribution (GSD) for various degrees of $\%R_x$ has been compared in Fig. 19-(b) where solid and dash lines represent random and cluster nuclei cases, respectively. Here, $P(n) := n_i/N$ is the frequency; where N is the total number of grains in the RVE; n_i is the number of grains in the size interval i; d is the average diameter of grain. From the comparison, one can see, that for relatively medium size d (i.e., in the range 40 μm ≤ d ≤ 70 μm), $P(n)$ reduces significantly for particular d with increasing $\%R_x$. It indicates that with a higher degree of SRX, relatively smaller grains coalesce to each other and rapid growth of SRX grains occurs. However, in the later stage of SRX, these grain starts to grow and the total number of grain

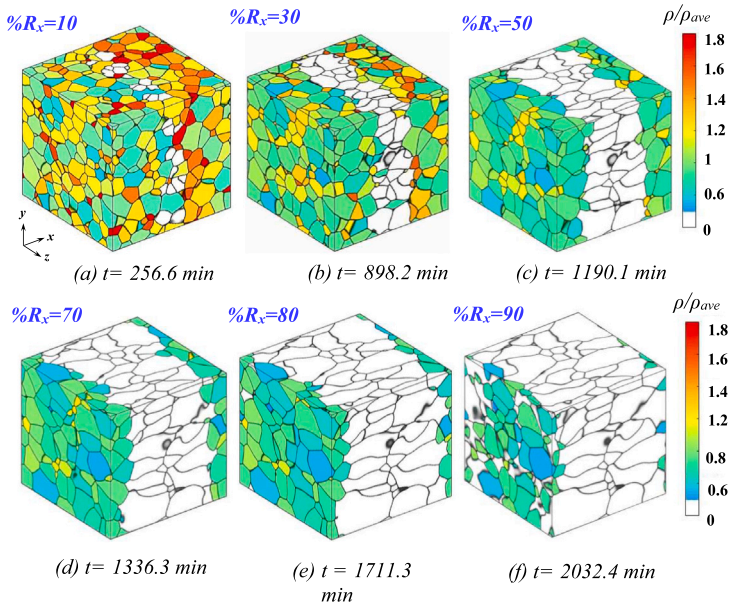

Fig. 18. Microstructural evolution in Ti-7Al during SRX at 800 °C for R_x: (a) 10%; (b) 30%; (c) 50%; (d) 70%; (e) 80%; (f) 90% in deformed ($\epsilon_{xx} = 20\%$) RVE cubic sample for banded nuclei distribution sites with CP-informed ρ/ρ_{ave}. SRX nuclei are positioned at the midsection of the x-axis, along the yz plane of the thickness of 1/8th of the sample size.

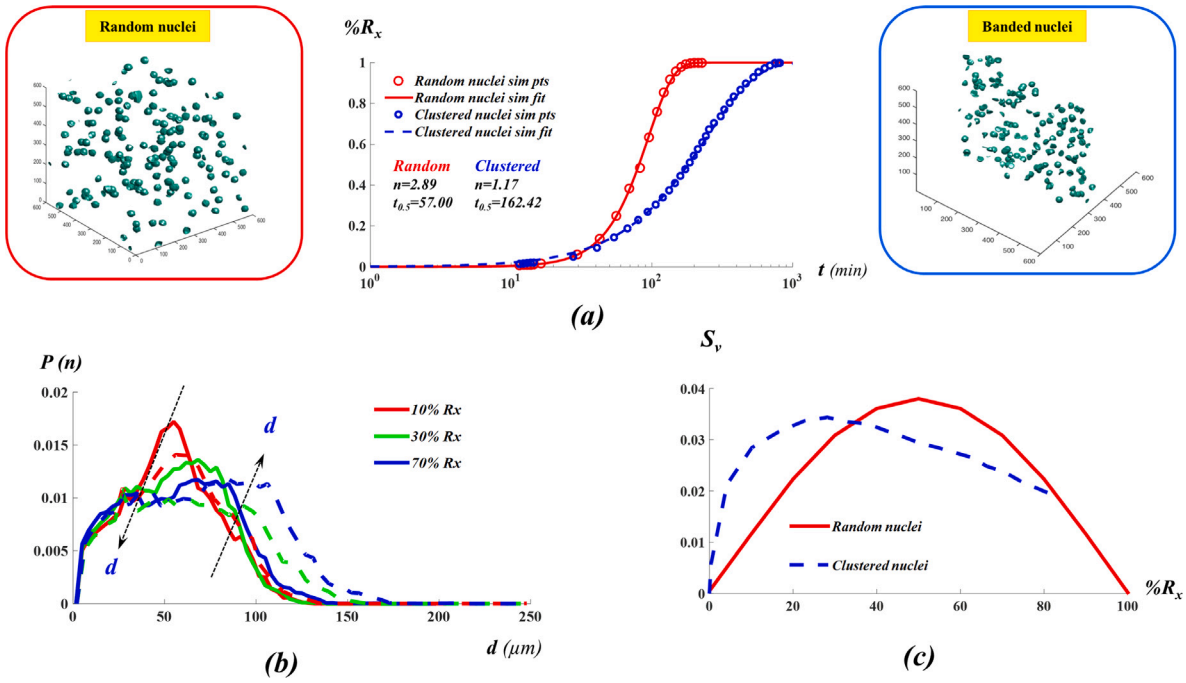

Fig. 19. The influence of nuclei impingement on the kinetics and microstructural parameters of SRX. Comparison of (a) $\%R_x$ vs t curve and Avirami parameters; (b) grain size distribution (GSD) curve for various $\%R_x$ value; (c) S_V vs $\%R_x$ curves between random nuclei case (solid line) and clustered nuclei case (dashed line).

in the RVE reduces which indicate the grain growth regime. For the cluster nuclei case, such a mechanism occurs earlier compared to the random nuclei case. This is due to a high degree of grain impingement which can be further characterized by free surface fraction analysis (see Section 6.7.3).

6.7.3. *Free surface fraction* (S_V)

To further characterize the degree of heterogeneity during SRX, an additional microstructural property called the free surface area fraction S_V [109,124] has been used. It measures the interfacial area density separating SRX grains from non-SRX grain volume (i.e., unimpinged, free-to-move grain boundaries) as a function of time and the transformation kinetics. The comparison of S_V vs. $\%R_x$ between random and cluster nuclei cases has been shown in Fig. 19-(c). At the initial stages of SRX, the SRX grains are relatively small which results in a small S_V value since the total area of grain boundaries is proportional to the SRX grain size. As time progresses, SRX grains begin to impinge on each other which leads to a decrease in the free surface fraction. Eventually, $S_V \rightarrow 0$ for $\%R_x \rightarrow 100$ as grain boundaries that separate SRX and non-SRX regions cease to exist. Thus, for randomly nucleated, site-saturated nucleation and growth transformations, S_V is found to be a symmetric bell-shaped curve with respect to R_x as shown in

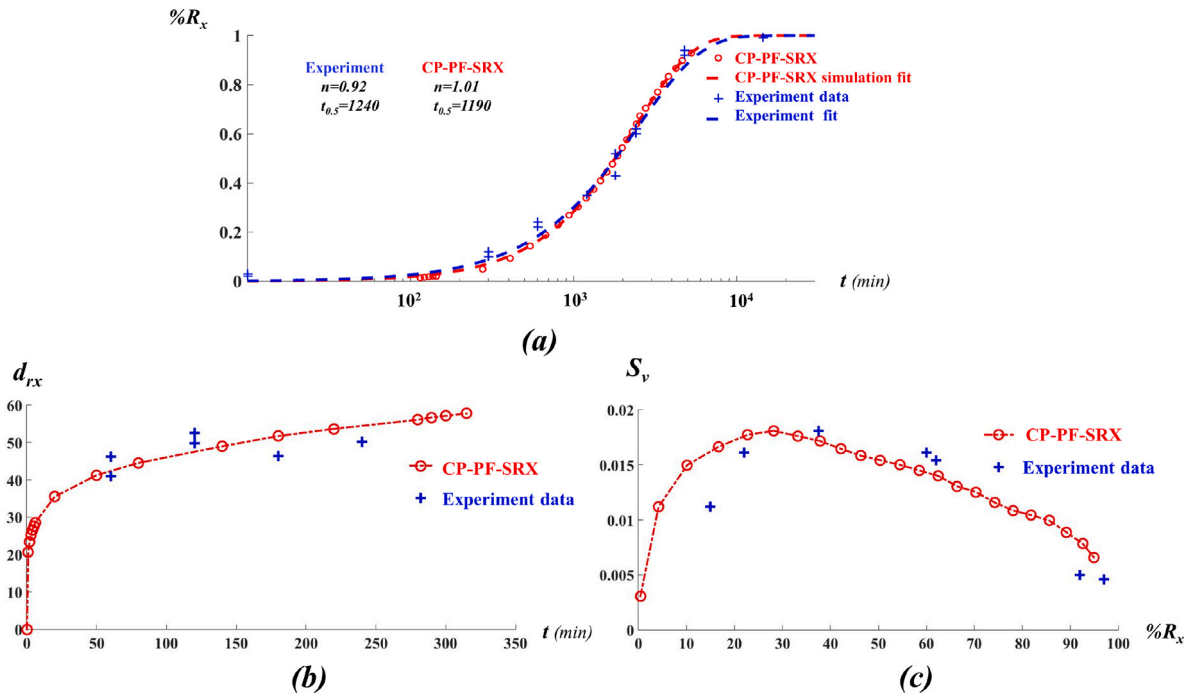

Fig. 20. Comparison between Ti-7Al experiment results and CP-PF-SRX simulation for (a) $\%R_x$ vs. t curve and Avirami parameters; (b) grain growth curve vs. annealing time (in min) ; (c) S_v vs. $\%R_x$ during SRX. CP-PF-SRX simulation results demonstrate excellent agreement with the experiment.

Fig. 19-(b). The obtained value of S_V for random nuclei case peaks at $\%R_x \approx 50$ which is consistent with the theoretical relationship between S_V and the fraction recrystallized [124]. However, for clustered nuclei arrangement, SRX begins to impinge on each other relatively early compared to random nuclei distribution. Therefore, for a such case, S_V vs. $\%R_x$ became asymmetric where peak of the curve S_V^{max} reaches before $\%R_x < 50$ as shown in Fig. 19-(b) In general, such a trend has also been observed in Aluminum [125] and Iron [124]. More specifically, S_v values for commercial aluminum alloy peak between $30 \leq \%R_x \leq 40$ for the presence of a cluster of SRX grains [125]. Furthermore, utilizing Eq. (16) from our geometric impingement theory, we predict $(R_x^{imp})^t = 37\%$ and $d^{\,t}_{imp} = 48.82$ μm and which is consist with simulation results $(R_x^{imp})^s \approx 30\%$ and $d^{\,t}_{imp} = 55$ μm from in Fig. 17 and Fig. 19-(c), respectively. The overall results for random and banded nuclei arrangement for Avrami exponent n, $t_{0.5}$, R^2, S_V^{max}, and $\%R_x^{S_v}$ from simulation results along with the theoretical predictions of $d^{\,t}_{imp}$ and $(R_x^{imp})^t$ are summarized in Table 3. In general, our framework can simulate the grain impingement physics and predict associated kinetics correctly illustrating the superior capability of the proposed CP-PF-SRX model for simulating the influence of nuclei clustering on SRX path kinetics.

6.8. Experimental comparison of SRX for Ti-7Al

In this section, the kinetics of SRX and grain growth from the simulation have been directly compared with the experimental observation for Ti-7Al. Since, in the Ti-7Al sample, nuclei clustering has been observed experimentally from partially recrystallized EBSD scans (as shown in Fig. 6- a, b), therefore, simulated SRX kinetics under initial clustering of nuclei has been compared with experimental results as shown in Fig. 20 -(a). The simulation results were then fit to the Avrami relationship that results in an Avrami time exponent of $n = 1.01$ with $t_{0.5} = 1190.00$ min which is an excellent agreement with the experimental result of $n = 0.92$ with $t_{0.5} = 1240.00$ min for Ti-7Al. Thus, by carefully characterizing the initial distribution of nuclei arrangement to be non-random, we can reproduce an accurate representation of SRX kinetics and Avirami exponent that closely matches the value that was measured experimentally.

Since SRX occurs during annealing that can also be associated with grain growth. Thus, the grain growth kinetics cannot be fully isolated as it can be compounded with the SRX. Therefore, in order to produce an equiaxed and fully SRX microstructure during the experiment, heat treatments have been performed before beginning the grain growth study [87]. Assuming circular grains, the mean linear intercept can be measured as $l = \sqrt{(\pi/4)A}$ where $A = \pi/4(d_{rx})^2$ is the average grain area, and d_{rx} is average grain diameter during grain growth. Typically, the grain growth kinetics can be expressed by $d_{rx} - d_0 = kt_g^n$ where d_0 is the initial grain size; k is a constant; n is the grain growth exponent which can be determined from the slope of a plot $\ln(d_{rx} - d_0)$ vs. $\ln(t)$. The resulting grain growth kinetics has been compared with the simulation results where d_{rx} is plotted versus t as shown in Fig. 20-(b). We can see that, with increasing t, d_{rx} increases with an initial steep slope indicating rapid grain growth followed by a decreasing slope that eventually approaches to steady state. This is due to the fact that an increase in d_{rx} leads to a reduction in the total grain boundary energy (i.e., lower driving force). Upon comparison, we obtain the value of $n_g = 0.29$ from our simulation which is in good agreement with the experimental value $n_g = 0.31$. In addition, the grain growth kinetics of α-Ti reported in [126] obtain $n_g = 0.50$ at 800 °C which is consistent with the results in this work.

In addition, we compare S_v vs. $\%R_x$ curves between our simulation and experiments as depicted in Fig. 20-(c). For clustered nuclei case, S_v curve demonstrates significant asymmetry with a maximum value of $(S_v)^{max} = 0.018$ at $\%R_X \simeq 28$. This peak value is slightly lower than that of the experimental observation of $(S_V)^{max} \simeq 0.016$. Compared to simulation prediction, the experimental S_v vs. $\%R_x$ have relatively high symmetricity which peak between $\%R_X \simeq 35$ and $\%R_X \simeq 40$. Thus, our framework can predict the influence of nuclei clustering on SRX path kinetics validating experimental results. Along the similar line, S_v values for commercial aluminum alloy peak between $30 \leq \%R_x \leq 40$ for the presence of a cluster of SRX grains [125]. In addition, GSD curves from the simulation for various degree of $\%R_x$ has been shown in Figs. 21-(a) and 21-(b) for random and cluster nuclei cases,

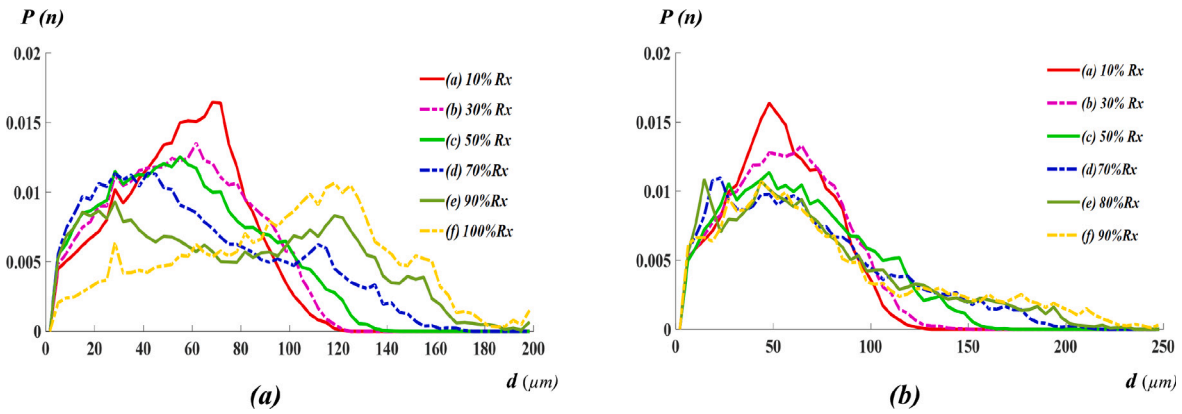

Fig. 21. Grain size distribution (GSD) curves for different $\%R_x$ for (a) random nuclei case; (b) clustered nuclei case in Ti-7Al during SRX at 800 °C.

Table 4
Overall results from the experiment, simulation for banded nuclei arrangement along with the theoretical predictions of d^{t}_{imp} and $(R_x^{imp})^t$ for Ti-7Al at 800 °C.

Cases	n	$t_{0.5}$ (in min)	R^2	S_V^{max}	$\%R_x^{S_v}$	d^{t}_{imp} (in μm)	$(R_x^{imp})^t$
Experiments	0.92	1240	0.89	$\simeq 0.016$	$35 \leq \%R_x \leq 40$	–	–
CP-PF-SRX	1.01	1190	0.91	0.018	28	48.82	37.00

respectively. From the distribution, we can conclude that, for the nuclei clustering case, impingement happens at $30 \leq \%(R_x^{imp}) \leq 40$ with $d_{imp} \simeq 0.016$. Furthermore, we predict $(R_x^{imp})^t = 37\%$ and $d^{t}_{imp} = 48.82\mu m$ from our geometric impingement theory which is consistent with both simulation and experimental results. Noteworthy to mention, experimental S_v vs. $\%R_x$ plot in Fig. 20-(c) indicates that impingement starts around $35 \leq \%(R_x) \leq 40$ (i.e, corresponding to $(S_v)^{max} \simeq 0.016$) which is well agreement with our theoretical prediction $(R_x^{imp})^t = 37\%$. The overall results from the experiment, simulation results for banded nuclei arrangement along with the theoretical predictions of d^{t}_{imp} and $(R_x^{imp})^t$ are summarized in Table 4. In comparison with experimental results, our framework validates growth kinetics for nuclei clustering as well as various morphological descriptors during SRX in Ti-7Al illustrating its superior capability of simulating SRX path kinetics.

7. Discussion

The present work demonstrated the efficacy of the proposed CP-PF-SRX model for predicting texture evolution during deformation as well as SRX kinetics and other important microstructural descriptors during annealing in Ti-alloys. For both Ti-0Al and Ti-7Al, the CP-PF-SRX model can reproduce experimental stress–strain behavior during the deformation process and predict the recrystallization texture. Based on experimentally observed microstructural heterogeneity and processing history, the SRX and grain growth have been quantified via Avirami kinetics compared with different impingement conditions corresponding to various nuclei distributions. For Ti-7Al, the experimental observation indicates the occurrence of in-homogeneous nuclei distribution in the form of band-shaped clusters. This leads to an anisotropic growth rate due to grain impingement during SRX, and, in turn, produces $n \approx 1$ which is significantly lower than the case for the random distribution of nuclei. In addition, it also reduces the peak value of Sv and breaks the symmetric nature of S_V vs. $\%R_x$ curve compared to randomly distributed nuclei. This is due to the impingement of SRX grain much earlier in the SRX process. Our simulation results reproduce such non-trivial SRX path kinetics and microstructural morphological descriptors accurately. However, the deviation of the predicted result and experimental observation can be attributed to inherent variability that exists in the initial nuclei distribution and material heterogeneity of the real material. In the actual material, clustered nuclei may not always exist in a repeating band as they are simulated in the CP-PF-SRX model. There can be the presence of heterogeneity in nuclei distribution where both random distributions, banded and globular clustering exist. Despite these variations, the proposed framework is able to capture the experimentally observed SRX kinetics correctly with good agreement with Avrami exponents, and, therefore, confirms our hypothesis that these inhomogeneities are the main cause of significant deviation of Avrami exponent. In short, we demonstrated that by carefully calibrating CP and PF parameters and altering the nuclei distribution from experimental characterization, our CP-PF-SRX model can accurately predict the non-trivial SRX kinetics as well as various microstructural descriptors. Future studies will focus on extending the proposed framework to model the DRX phenomenon for various strain rate conditions [127]. In addition, grain boundary formulation can be implanted in the proposed framework to further improve the CP-PF-SRX model. Furthermore, the predictive capability of stress–strain response can be further improved by various data-driven deep learning-based constitutive modeling approaches [128–132]. Finally, thermodynamically-consistent PF models [133–137] can be employed to further improve the microstructure evolution and kinetic prediction during the SRX process.

8. Conclusion

Summarizing, in the present work, we present a three-dimensional integrated computational materials engineering framework for predicting post-deformation texture and SRX kinetics during hot-forming in Ti-alloys. To achieve these objectives, we combine CP and PF models where CP models provide the evolution of grain-scale deformation, dislocation density, and grain orientation. Whereas, the PF model provides temporal evolution of SRX microstructure and kinetics of grain growth utilizing CP-informed stored energy. We have further explored experimentally-informed microstructural inhomogeneity in terms of nuclei distribution for different Ti-alloys. For various nuclei arrangements, the evolution of non-trivial SRX grain morphology, kinetics, and various microstructural path descriptors have been compared and directly validated with the experimental observations. It has been shown that the proposed framework can capture the post-deformation grain orientation correctly as well as experimentally observed SRX

kinetics with excellent agreement with Avrami exponents. In short, we demonstrated that by carefully calibrating CP and PF parameters and altering the nuclei distribution from experimental characterization, the proposed CP-PF-SRX model can accurately predict the non-trivial SRX kinetics as well as various microstructural descriptors during SRX.

Declaration of competing interest

The authors declare that they have no known competing financial interests or personal relationships that could have appeared to influence the work reported in this paper.

Data availability

The data that support the findings of this study are available from the author upon reasonable request.

Acknowledgments

The experimental work presented here was funded by Office of Naval Research (ONR), USA grant N00014-12-1-0013 and was performed by Dr. Anna Trump and Dr. John Allison from Materials Science and Engineering at University of Michigan. The authors are grateful to Dr. Susan P. Gentry from Materials Science and Engineering at the University of California, Davis and Dr. Katsuyo Thronton from Materials Science and Engineering at University of Michigan for their kind guidance and assistance. The experimental data presented in this paper was collected and analyzed by Dr. Anna Trump during her doctoral research. The computations have been carried out as part of research supported by the U.S. Department of Energy, Office of Basic Energy Sciences, Division of Materials Sciences and Engineering under Award no. DE-SC0008637 funds the Predictive Integrated Structural Materials Science (PRISMS) Center at the University of Michigan, USA. RA acknowledges the support of National Science Foundation (NSF), USA through Grant No. 2119103.

References

[1] M. Zhang, J. Zhang, D. McDowell, Microstructure-based crystal plasticity modeling of cyclic deformation of Ti–6Al–4V, Int. J. Plast. 23 (8) (2007) 1328–1348.
[2] X. Fan, H. Yang, Internal-state-variable based self-consistent constitutive modeling for hot working of two-phase titanium alloys coupling microstructure evolution, Int. J. Plast. 27 (11) (2011) 1833–1852.
[3] F.J. Humphreys, M. Hatherly, Recrystallization and Related Annealing Phenomena, Elsevier, 2012.
[4] D. Raabe, F. Roters, F. Barlat, L.-Q. Chen, Continuum Scale Simulation of Engineering Materials: Fundamentals-Microstructures-Process Applications, John Wiley & Sons, 2004.
[5] C. Yan, A. Feng, S. Qu, G. Cao, J. Sun, J. Shen, D. Chen, Dynamic recrystallization of titanium: Effect of pre-activated twinning at cryogenic temperature, Acta Mater. 154 (2018) 311–324.
[6] C.K. Lieou, C.A. Bronkhorst, Dynamic recrystallization in adiabatic shear banding: Effective-temperature model and comparison to experiments in ultrafine-grained titanium, Int. J. Plast. 111 (2018) 107–121.
[7] K. Min, W. Jeong, S. Hong, C. Lee, P.-R. Cha, H. Han, M.-G. Lee, Integrated crystal plasticity and phase field model for prediction of recrystallization texture and anisotropic mechanical properties of cold-rolled ultra-low carbon steels, Int. J. Plast. 127 (2020) 102644.
[8] S.-F. Chen, K. Bandyopadhyay, S. Basak, B. Hwang, J.-H. Shim, J. Lee, M.-G. Lee, Predictive integrated numerical approach for modeling spatio-temporal microstructure evolutions and grain size dependent phase transformations in steels, Int. J. Plast. 139 (2021) 102952.
[9] M.T. Tran, H. Wang, H.W. Lee, D.-K. Kim, Crystal plasticity finite element analysis of size effect on the formability of ultra-thin ferritic stainless steel sheet for fuel cell bipolar plate, Int. J. Plast. 154 (2022) 103298.
[10] A.S. Khan, R. Kazmi, B. Farrokh, Multiaxial and non-proportional loading responses, anisotropy and modeling of Ti–6Al–4V titanium alloy over wide ranges of strain rates and temperatures, Int. J. Plast. 23 (6) (2007) 931–950.
[11] J.H. Sung, J.H. Kim, R. Wagoner, A plastic constitutive equation incorporating strain, strain-rate, and temperature, Int. J. Plast. 26 (12) (2010) 1746–1771.
[12] Q. Luan, J. Lee, J.-H. Zheng, C. Hopper, J. Jiang, Combining microstructural characterization with crystal plasticity and phase-field modelling for the study of static recrystallization in pure aluminium, Comput. Mater. Sci. 173 (2020) 109419.
[13] J. Allison, D. Backman, L. Christodoulou, Integrated computational materials engineering: A new paradigm for the global materials profession, Jom 58 (11) (2006) 25–27.
[14] A. Arsenlis, D.M. Parks, Modeling the evolution of crystallographic dislocation density in crystal plasticity, J. Mech. Phys. Solids 50 (9) (2002) 1979–2009.
[15] F. Roters, P. Eisenlohr, T.R. Bieler, D. Raabe, Crystal Plasticity Finite Element Methods: in Materials Science and Engineering, John Wiley & Sons, 2011.
[16] K.-S. Cheong, E.P. Busso, Discrete dislocation density modelling of single phase FCC polycrystal aggregates, Acta Mater. 52 (19) (2004) 5665–5675.
[17] A. Ma, F. Roters, D. Raabe, A dislocation density based constitutive model for crystal plasticity FEM including geometrically necessary dislocations, Acta Mater. 54 (8) (2006) 2169–2179.
[18] I. Beyerlein, C. Tomé, A dislocation-based constitutive law for pure Zr including temperature effects, Int. J. Plast. 24 (5) (2008) 867–895.
[19] M. Lee, H. Lim, B. Adams, J. Hirth, R. Wagoner, A dislocation density-based single crystal constitutive equation, Int. J. Plast. 26 (7) (2010) 925–938.
[20] H. Lim, L. Hale, J. Zimmerman, C. Battaile, C. Weinberger, A multi-scale model of dislocation plasticity in α-Fe: Incorporating temperature, strain rate and non-schmid effects, Int. J. Plast. 73 (2015) 100–118.
[21] M. Zecevic, M. Knezevic, A dislocation density based elasto-plastic self-consistent model for the prediction of cyclic deformation: Application to AA6022-T4, Int. J. Plast. 72 (2015) 200–217.
[22] F. Roters, P. Eisenlohr, L. Hantcherli, D.D. Tjahjanto, T.R. Bieler, D. Raabe, Overview of constitutive laws, kinematics, homogenization and multiscale methods in crystal plasticity finite-element modeling: Theory, experiments, applications, Acta Mater. 58 (4) (2010) 1152–1211.
[23] M.E. Nixon, O. Cazacu, R.A. Lebensohn, Anisotropic response of high-purity α-titanium: Experimental characterization and constitutive modeling, Int. J. Plast. 26 (4) (2010) 516–532.
[24] S. Ghosh, M. Anahid, Homogenized constitutive and fatigue nucleation models from crystal plasticity FE simulations of Ti alloys, part 1: Macroscopic anisotropic yield function, Int. J. Plast. 47 (2013) 182–201.
[25] M. Anahid, S. Ghosh, Homogenized constitutive and fatigue nucleation models from crystal plasticity FE simulations of Ti alloys, part 2: Macroscopic probabilistic crack nucleation model, Int. J. Plast. 48 (2013) 111–124.
[26] S.R. Niezgoda, A.K. Kanjarla, I.J. Beyerlein, C.N. Tomé, Stochastic modeling of twin nucleation in polycrystals: An application in hexagonal close-packed metals, Int J Plast 56 (2014) 119–138.
[27] B. Feng, C.A. Bronkhorst, Z. Liu, B.M. Morrow, E. Cerreta, W. Li, N. Daphalapurkar, Three-dimensional modeling and simulations of single-crystal and bi-crystal titanium for high-strain-rate loading conditions, Int. J. Plast. 133 (2020) 102771.
[28] H. Li, C. Wu, H. Yang, Crystal plasticity modeling of the dynamic recrystallization of two-phase titanium alloys during isothermal processing, Int. J. Plast. (51) (2013) 271–291.
[29] Z. Zheng, D.S. Balint, F.P. Dunne, Dwell fatigue in two Ti alloys: An integrated crystal plasticity and discrete dislocation study, J. Mech. Phys. Solids 96 (2016) 411–427.
[30] Z. Zhang, T.-S. Jun, T.B. Britton, F.P. Dunne, Determination of Ti-6242 α and β slip properties using micro-pillar test and computational crystal plasticity, J. Mech. Phys. Solids 95 (2016) 393–410.
[31] T. Ozturk, A.D. Rollett, Effect of microstructure on the elasto-viscoplastic deformation of dual phase titanium structures, Comput. Mech. 61 (1) (2018) 55–70.
[32] K. Kapoor, Y.S.J. Yoo, T.A. Book, J.P. Kacher, M.D. Sangid, Incorporating grain-level residual stresses and validating a crystal plasticity model of a two-phase Ti-6Al-4 V alloy produced via additive manufacturing, J. Mech. Phys. Solids 121 (2018) 447–462.
[33] Z. Zheng, S. Waheed, D.S. Balint, F.P. Dunne, Slip transfer across phase boundaries in dual phase titanium alloys and the effect on strain rate sensitivity, Int. J. Plast. 104 (2018) 23–38.
[34] R.A. Lebensohn, A.K. Kanjarla, P. Eisenlohr, An elasto-viscoplastic formulation based on fast Fourier transforms for the prediction of micromechanical fields in polycrystalline materials, Int. J. Plast. 32 (2012) 59–69.
[35] P. Eisenlohr, M. Diehl, R.A. Lebensohn, F. Roters, A spectral method solution to crystal elasto-viscoplasticity at finite strains, Int. J. Plast. 46 (2013) 37–53.
[36] H. Bunge, Texture analysis in materials ScienceButterworths, London 11 (1982) L0.
[37] U.F. Kocks, C.N. Tomé, H.-R. Wenk, texture and Anisotropy: Preferred Orientations in Polycrystals and Their Effect on Materials Properties, Cambridge University Press, 1998.
[38] A. Heinz, P. Neumann, Representation of orientation and disorientation data for cubic, hexagonal, tetragonal and orthorhombic crystals, Acta Crystallogr. A: Found Crystallogr. 47 (6) (1991) 780–789.
[39] B.L. Adams, A. Henrie, B. Henrie, M. Lyon, S. Kalidindi, H. Garmestani, Microstructure-sensitive design of a compliant beam, J. Mech. Phys. Solids 49 (8) (2001) 1639–1663.

[40] S.R. Kalidindi, J.R. Houskamp, M. Lyons, B.L. Adams, Microstructure sensitive design of an orthotropic plate subjected to tensile load, Int. J. Plast. 20 (8–9) (2004) 1561–1575.

[41] A. Kumar, P. Dawson, Computational modeling of FCC deformation textures over Rodrigues' space, Acta Mater. 48 (10) (2000) 2719–2736.

[42] A. Kumar, P.R. Dawson, Modeling crystallographic texture evolution with finite elements over neo-Eulerian orientation spaces, Comput. Methods Appl. Mech. Engrg. 153 (3–4) (1998) 259–302.

[43] P. Acar, V. Sundararaghavan, Uncertainty quantification of microstructural properties due to variability in measured pole figures, Acta Mater. 124 (2017) 100–108.

[44] P. Acar, A. Ramazani, V. Sundararaghavan, Crystal plasticity modeling and experimental validation with an orientation distribution function for Ti-7Al alloy, Metals 7 (11) (2017) 459.

[45] M. Hasan, P. Acar, Uncertainty quantification of metallic microstructures with analytical and machine learning based approaches, AIAA J. 60 (1) (2022) 461–472.

[46] P. Acar, Recent progress of uncertainty quantification in small-scale materials science, Prog. Mater. Sci. 117 (2021) 100723.

[47] P. Acar, Machine learning reinforced crystal plasticity modeling under experimental uncertainty, AIAA J. 58 (8) (2020) 3569–3576.

[48] P. Acar, Uncertainty quantification for Ti-7Al alloy microstructure with an inverse analytical model (AUQLin), Materials 12 (11) (2019) 1773.

[49] P. Acar, V. Sundararaghavan, Stochastic design optimization of microstructural features using linear programming for robust design, AIAA J. 57 (1) (2019) 448–455.

[50] P. Acar, S. Srivastava, V. Sundararaghavan, Stochastic design optimization of microstructures with utilization of a linear solver, AIAA J. 55 (9) (2017) 3161–3168.

[51] E.A. Holm, M.A. Miodownik, A.D. Rollett, On abnormal subgrain growth and the origin of recrystallization nuclei, Acta Mater. 51 (9) (2003) 2701–2716.

[52] M.H. Alvi, S. Cheong, J. Suni, H. Weiland, A. Rollett, Cube texture in hot-rolled aluminum alloy 1050 (AA1050)—nucleation and growth behavior, Acta Mater. 56 (13) (2008) 3098–3108.

[53] M.S. Salehi, S. Serajzadeh, Simulation of static recrystallization in non-isothermal annealing using a coupled cellular automata and finite element model, Comput. Mater. Sci. 53 (1) (2012) 145–152.

[54] L. Wang, G. Fang, L. Qian, Modeling of dynamic recrystallization of magnesium alloy using cellular automata considering initial topology of grains, Mater. Sci. Eng. A 711 (2018) 268–283.

[55] I. Steinbach, Phase-field model for microstructure evolution at the mesoscopic scale, Annu. Rev. Mater. Res. 43 (2013) 89–107.

[56] D. Tourret, H. Liu, J. LLorca, Phase-field modeling of microstructure evolution: Recent applications, perspectives and challenges, Prog. Mater. Sci. 123 (2022) 100810.

[57] M.R. Tonks, L.K. Aagesen, The phase field method: Mesoscale simulation aiding material discovery, Annu. Rev. Mater. Res. 49 (2019) 79–102.

[58] A.M. Roy, Multiphase phase-field approach for solid–solid phase transformations via propagating interfacial phase in HMX, J. Appl. Phys. 129 (2) (2021) 025103.

[59] A.M. Roy, Barrierless melt nucleation at solid-solid interface in energetic nitramine octahydro-1, 3, 5, 7-tetranitro-1, 3, 5, 7-tetrazocine, Materialia 15 (2021) 101000.

[60] A.M. Roy, Formation and stability of nanosized, undercooled propagating intermediate melt during $\beta \rightarrow \delta$ phase transformation in HMX nanocrystal, Europhys. Lett. 133 (5) (2021) 56001.

[61] A.M. Roy, Energetics and kinematics of undercooled nonequilibrium interfacial molten layer in cyclotetramethylene-tetranitramine crystal, Physica B 615 (2021) 412986.

[62] A.M. Roy, Influence of nanoscale parameters on solid–solid phase transformation in octogen crystal: Multiple solution and temperature effect, JETP Lett. 113 (4) (2021) 265–272.

[63] L. Gránásy, L. Rátkai, A. Szállás, B. Korbuly, G.I. Tóth, L. Környei, T. Pusztai, Phase-field modeling of polycrystalline solidification: From needle crystals to spherulites—A review, Metall. Mater. Trans. A 45 (4) (2014) 1694–1719.

[64] T. Takaki, Y. Hisakuni, T. Hirouchi, A. Yamanaka, Y. Tomita, Multi-phase-field simulations for dynamic recrystallization, Comput. Mater. Sci. 45 (4) (2009) 881–888.

[65] T. Takaki, Y. Tomita, Static recrystallization simulations starting from predicted deformation microstructure by coupling multi-phase-field method and finite element method based on crystal plasticity, Int. J. Mech. Sci. 52 (2) (2010) 320–328.

[66] B. Zhu, M. Militzer, 3D phase field modelling of recrystallization in a low-carbon steel, Modelling Simul. Mater. Sci. Eng. 20 (8) (2012) 085011.

[67] Y. Suwa, Y. Saito, H. Onodera, Phase-field simulation of recrystallization based on the unified subgrain growth theory, Comput. Mater. Sci. 44 (2) (2008) 286–295.

[68] S. Gentry, K. Thornton, Simulating recrystallization in titanium using the phase field method, IOP Conf. Ser.: Mater. Sci. Eng. 89 (1) (2015) 012024.

[69] S.P. Gentry, K. Thornton, Sensitivity analysis of a phase field model for static recrystallization of deformed microstructures, Modelling Simul. Mater. Sci. Eng. 28 (6) (2020) 065002.

[70] S. Hu, L. Chen, A phase-field model for evolving microstructures with strong elastic inhomogeneity, Acta Mater. 49 (11) (2001) 1879–1890.

[71] C. Krill Iii, L.-Q. Chen, Computer simulation of 3-D grain growth using a phase-field model, Acta Mater. 50 (12) (2002) 3059–3075.

[72] L.-Q. Chen, Phase-field models for microstructure evolution, Annu. Rev. Mater. Sci. 32 (1) (2002) 113–140.

[73] I. Steinbach, Phase-field models in materials science, Model. Simul. Mater. Sci. Eng. 17 (7) (2009) 073001.

[74] N. Moelans, B. Blanpain, P. Wollants, Quantitative phase-field approach for simulating grain growth in anisotropic systems with arbitrary inclination and misorientation dependence, Phys. Rev. Lett. 101 (2) (2008) 025502.

[75] N. Moelans, B. Blanpain, P. Wollants, Quantitative analysis of grain boundary properties in a generalized phase field model for grain growth in anisotropic systems, Phys. Rev. B 78 (2) (2008) 024113.

[76] N. Moelans, A quantitative and thermodynamically consistent phase-field interpolation function for multi-phase systems, Acta Mater. 59 (3) (2011) 1077–1086.

[77] N. Moelans, A. Godfrey, Y. Zhang, D.J. Jensen, Phase-field simulation study of the migration of recrystallization boundaries, Phys. Rev. B 88 (5) (2013) 054103.

[78] P. Zhao, T.S.E. Low, Y. Wang, S.R. Niezgoda, An integrated full-field model of concurrent plastic deformation and microstructure evolution: Application to 3D simulation of dynamic recrystallization in polycrystalline copper, Int. J. Plast. 80 (2016) 38–55.

[79] P. Zhao, Y. Wang, S.R. Niezgoda, Microstructural and micromechanical evolution during dynamic recrystallization, Int. J. Plast. 100 (2018) 52–68.

[80] D. Raabe, R.C. Becker, Coupling of a crystal plasticity finite-element model with a probabilistic cellular automaton for simulating primary static recrystallization in aluminium, Modelling Simul. Mater. Sci. Eng. 8 (4) (2000) 445.

[81] B. Radhakrishnan, G. Sarma, H. Weiland, P. Baggethun, Simulations of deformation and recrystallization of single crystals of aluminium containing hard particles, Modelling Simul. Mater. Sci. Eng. 8 (5) (2000) 737.

[82] B. Radhakrishnan, G. Sarma, The effect of coarse non-deformable particles on the deformation and static recrystallization of aluminium alloys, Phil. Mag. 84 (22) (2004) 2341–2366.

[83] T.-L. Cheng, Y.-H. Wen, J.A. Hawk, Diffuse interface approach to modeling crystal plasticity with accommodation of grain boundary sliding, Int. J. Plast. 114 (2019) 106–125.

[84] A. Ask, S. Forest, B. Appolaire, K. Ammar, O.U. Salman, A cosserat crystal plasticity and phase field theory for grain boundary migration, J. Mech. Phys. Solids 115 (2018) 167–194.

[85] Y. Li, S. Hu, E. Barker, N. Overman, S. Whalen, S. Mathaudhu, Effect of grain structure and strain rate on dynamic recrystallization and deformation behavior: A phase field-crystal plasticity model, Comput. Mater. Sci. 180 (2020) 109707.

[86] A. Vondrous, P. Bienger, S. Schreijäg, M. Selzer, D. Schneider, B. Nestler, D. Helm, R. Mönig, Combined crystal plasticity and phase-field method for recrystallization in a process chain of sheet metal production, Comput. Mech. 55 (2) (2015) 439–452.

[87] A.M. Trump, J.E. Allison, The influence of aluminum concentration on static recrystallization in alpha titanium alloys, in: Proceedings of the 13th World Conference on Titanium, Wiley Online Library, 2016, pp. 695–696.

[88] E. Villa, P.R. Rios, Transformation kinetics for nucleus clusters, Acta Mater. 57 (13) (2009) 3714–3724.

[89] P.S. De, A. Vuppuluri, S.S. Vadlamani, S. Vedantam, A physically based model of the effect of recovery and clustering on recrystallization kinetics, J. Mater. Sci. 56 (11) (2021) 7082–7093.

[90] M. Yaghoobi, S. Ganesan, S. Sundar, A. Lakshmanan, S. Rudraraju, J.E. Allison, V. Sundararaghavan, PRISMS-plasticity: An open-source crystal plasticity finite element software, Comput. Mater. Sci. 169 (2019) 109078.

[91] L. Aagesen, J. Adams, J. Allison, W. Andrews, V. Araullo-Peters, T. Berman, Z. Chen, S. Daly, S. Das, S. DeWitt, et al., Prisms: An integrated, open-source framework for accelerating predictive structural materials science, JOM 70 (10) (2018) 2298–2314.

[92] L. Anand, M. Kothari, A computational procedure for rate-independent crystal plasticity, J. Mech. Phys. Solids 44 (4) (1996) 525–558.

[93] G. Lütjering, J.C. Williams, Titanium, Springer Science & Business Media, 2007.

[94] S. Balasubramanian, L. Anand, Plasticity of initially textured hexagonal polycrystals at high homologous temperatures: Application to titanium, Acta Mater. 50 (1) (2002) 133–148.

[95] L. Nervo, A. King, A. Fitzner, W. Ludwig, M. Preuss, A study of deformation twinning in a titanium alloy by X-ray diffraction contrast tomography, Acta Mater. 105 (2016) 417–428.

[96] J. Williams, R. Baggerly, N. Paton, Deformation behavior of HCP Ti-Al alloy single crystals, Metall. Mater. Trans. A 33 (3) (2002) 837–850.

[97] U. Lienert, M. Brandes, J.V. Bernier, J. Weiss, S. Shastri, M. Mills, M. Miller, In situ single-grain peak profile measurements on Ti–7Al during tensile deformation, Mater. Sci. Eng. A 524 (1–2) (2009) 46–54.

[98] N. Paton, R. Baggerly, J. Williams, Rockwell international. AFOSR final report, 1976, Khan, AS, Kazmia, R., Farrokha, B. and Zupana, M., Int. J. Plast. 23 (2007) 1105–1125.

[99] A. Fitzner, D.L. Prakash, J.Q. Da Fonseca, M. Thomas, S.-Y. Zhang, J. Kelleher, P. Manuel, M. Preuss, The effect of aluminium on twinning in binary alpha-titanium, Acta Mater. 103 (2016) 341–351.

[100] T. Takaki, T. Hirouchi, Y. Hisakuni, A. Yamanaka, Y. Tomita, Multi-phase-field model to simulate microstructure evolutions during dynamic recrystallization, Mater. Trans. 49 (11) (2008) 2559–2565.

[101] S.M. Allen, J.W. Cahn, A microscopic theory for antiphase boundary motion and its application to antiphase domain coarsening, Acta Metall. 27 (6) (1979) 1085–1095.

[102] G. Wu, D.J. Jensen, Orientations of recrystallization nuclei developed in columnar-grained Ni at triple junctions and a high-angle grain boundary, Acta Mater. 55 (15) (2007) 4955–4964.

[103] A. Jokisaari, C. Permann, K. Thornton, A nucleation algorithm for the coupled conserved–nonconserved phase field model, Comput. Mater. Sci. 112 (2016) 128–138.

[104] J. Gruber, N. Ma, Y. Wang, A.D. Rollett, G.S. Rohrer, Sparse data structure and algorithm for the phase field method, Model. Simul. Mater. Sci. Eng. 14 (7) (2006) 1189.

[105] S. Vedantam, B. Patnaik, Efficient numerical algorithm for multiphase field simulations, Phys. Rev. E 73 (1) (2006) 016703.

[106] I. McKenna, S. Poulsen, E.M. Lauridsen, W. Ludwig, P.W. Voorhees, Grain growth in four dimensions: A comparison between simulation and experiment, Acta Mater. 78 (2014) 125–134.

[107] J.J. Jonas, X. Quelennec, L. Jiang, É. Martin, The Avrami kinetics of recrystallization, Acta Mater. 57 (9) (2009) 2748–2756.

[108] D. Martin, Application of Kolmogorov–Johnson–Mehl–Avrami equations to non-isothermal conditions, Comput. Mater. Sci. 47 (3) (2010) 796–800.

[109] R. Vandermeer, Microstructural descriptors and the effects of nuclei clustering on recrystallization path kinetics, Acta Mater. 53 (5) (2005) 1449–1457.

[110] M. Oyarzábal, A. Martínez-de Guerenu, I. Gutiérrez, Effect of stored energy and recovery on the overall recrystallization kinetics of a cold rolled low carbon steel, Mater. Sci. Eng. A 485 (1–2) (2008) 200–209.

[111] Z. Aretxabaleta, B. Pereda, B. López, Analysis of the effect of Al on the static softening kinetics of C-Mn steels using a physically based model, Metall. Mater. Trans. A 45 (2014) 934–947.

[112] K. Deb, A. Pratap, S. Agarwal, T. Meyarivan, A fast and elitist multiobjective genetic algorithm: NSGA-II, IEEE Trans. Evol. Comput. 6 (2) (2002) 182–197.

[113] A. Salem, S. Kalidindi, S. Semiatin, Strain hardening due to deformation twinning in α-titanium: Constitutive relations and crystal-plasticity modeling, Acta Mater. 53 (12) (2005) 3495–3502.

[114] E. Rigoni, A. Turco, Metamodels for fast multi-objective optimization: trading off global exploration and local exploitation, in: Simulated Evolution and Learning: 8th International Conference, SEAL 2010, Kanpur, India, December 1-4, 2010. Proceedings 8, Springer, 2010, pp. 523–532.

[115] W. Sha, S. Malinov, Titanium Alloys: Modelling of Microstructure, Properties and Applications, Elsevier, 2009.

[116] P. Acar, Crystal plasticity model calibration for Ti-7Al alloy with a multi-fidelity computational scheme, Integr. Mater. Manuf. Innov. 7 (4) (2018) 186–194.

[117] S. Ganesan, I. Javaheri, V. Sundararaghavan, Constrained Voronoi models for interpreting surface microstructural measurements, Mech. Mater. 159 (2021) 103892.

[118] S. Ganesan, M. Yaghoobi, A. Githens, Z. Chen, S. Daly, J.E. Allison, V. Sundararaghavan, The effects of heat treatment on the response of WE43 Mg alloy: crystal plasticity finite element simulation and SEM-DIC experiment, Int. J. Plast. 137 (2021) 102917.

[119] S. Ganesan, Microstructural Response of Magnesium Alloys: 3d Crystal Plasticity and Experimental Validation (Ph.D. thesis), 2017.

[120] Q. Sun, Q. Guo, X. Yao, L. Xiao, J.R. Greer, J. Sun, Size effects in strength and plasticity of single-crystalline titanium micropillars with prismatic slip orientation, Scr. Mater. 65 (6) (2011) 473–476.

[121] V. Sundararaghavan, N. Zabaras, Linear analysis of texture–property relationships using process-based representations of Rodrigues space, Acta Mater. 55 (5) (2007) 1573–1587.

[122] A. Trump, Recrystallization and Grain Growth Kinetics in Binary Alpha Titanium-Aluminum Alloys (Ph.D. thesis), 2017.

[123] Y. Lü, D.A. Molodov, G. Gottstein, Recrystallization kinetics and microstructure evolution during annealing of a cold-rolled Fe–Mn–C alloy, Acta Mater. 59 (8) (2011) 3229–3243.

[124] R.B. Godiksen, P.R. Rios, R.A. Vandermeer, S. Schmidt, D.J. Jensen, Three-dimensional geometric simulations of random anisotropic growth during transformation phenomena, Scr. Mater. 58 (4) (2008) 279–282.

[125] R. Vandermeer, D.J. Jensen, Recrystallization in hot vs cold deformed commercial aluminum: A microstructure path comparison, Acta Mater. 51 (10) (2003) 3005–3018.

[126] F. Gil, J. Picas, J. Manero, A. Forn, J. Planell, Effect of the addition of palladium on grain growth kinetics of pure titanium, J. Alloys Compd. 260 (1–2) (1997) 147–152.

[127] A.M. Roy, R. Arróyave, V. Sundararaghavan, Incorporating dynamic recrystallization into a crystal plasticity model for high-temperature deformation of Ti-6Al-4V, Mater. Sci. Eng. A (2023) 145211.

[128] A.M. Roy, R. Bose, V. Sundararaghavan, R. Arróyave, Deep learning-accelerated computational framework based on physics informed neural network for the solution of linear elasticity, Neural Netw. 162 (2023) 472–489.

[129] A.M. Roy, R. Bose, Physics-aware deep learning framework for linear elasticity, 2023, arXiv preprint arXiv:2302.09668.

[130] A.M. Roy, S. Guha, A data-driven physics-constrained deep learning computational framework for solving von mises plasticity, Eng. Appl. Artif. Intell. 122 (2023) 106049.

[131] A.M. Roy, S. Guha, Elastoplastic physics-informed deep learning approach for J2 plasticity, 2022, Available at SSRN 4332254.

[132] R. Bose, A.M. Roy, Invariance embedded physics-infused deep neural network-based sub-grid scale models for turbulent flows, Eng. Appl. Artif. Intell. 128 (2024) 107483.

[133] V.I. Levitas, A.M. Roy, D.L. Preston, Multiple twinning and variant-variant transformations in martensite: phase-field approach, Physical Review B 88 (5) (2013) 054113.

[134] V.I. Levitas, A.M. Roy, Multiphase phase field theory for temperature-and stress-induced phase transformations, Physical Review B 91 (17) (2015) 174109.

[135] V.I. Levitas, A.M. Roy, Multiphase phase field theory for temperature-induced phase transformations: formulation and application to interfacial phases, Acta Materialia 105 (2016) 244–257.

[136] A.M. Roy, Influence of interfacial stress on microstructural evolution in NiAl alloys, JETP Letters 112 (3) (2020) 173–179.

[137] A.M. Roy, Effects of interfacial stress in phase field approach for martensitic phase transformation in NiAl shape memory alloys, Applied Physics A 126 (7) (2020) 1–12.